

Deanship of Graduate Studies

Al-Quds University



Polyoxopalladates on Au (111) and HOPG substrates

Mahmoud Joma Zeer

M.Sc. Thesis

Jerusalem- Palestine

1435/2014

Deanship of Graduate studies

Al-Quds University



Polyoxopalladates on Au (111) and HOPG substrates

Prepared by

Mahmoud Joma Zeer

Supervisors:

Dr. Salman M. Salman

Physics Department, Alquds University, Palestine

PD Dr. Daniel E. Bürgler

Peter Grünberg Institute, Electronic Properties (PGI-6)
Jülich Research Center, Germany

Submitted in Partial Fulfillment of Requirements for
The Degree of Master of Science in Physics

Al-Quds University

Jerusalem-Palestine

1435/2014

**Deanship of Graduate Studies
Al-Quds University**



Polyoxopalladates on Au (111) and HOPG substrates

Thesis Approval

Prepared by

Mahmoud Joma Zeer
Registration No: 20920247

Supervisors

Dr. Salman M Salman, Physics Alquds University, Palestine.
PD Dr. Daniel E. Bürgler, Peter G \ddot{u} enberg Institute-PGI-6, FZ J \ddot{u} lich, Germany.

Master thesis submitted and accepted, date 20/ 5 /2014

Name and Signatures of the Examining Committee Members are as follows

Chairman of the Committee: Dr. Salman M Salman	Signature:.....
Internal Examiner: Dr. Musa Abu Tair	Signature:.....
External Examiner: Dr. Jamal Ghaboun	Signature:.....

**Jerusalem-Palestine
1435/2014**

Dedication

I dedicate this thesis to my family, especially, to my late father, to my mother for her patience and understanding and to my brothers and sisters, to my fiancé Walaa Adwan for opening my eyes to the world.

To the soul that hugs my soul, to the heart that pours secrets in my heart, to the hand that lit my emotions, to the faith that is considered the frame of my love I present this Work.

Declaration

I hereby declare that this thesis is based on the results found by myself. Materials and work conducted at Jülich. This thesis, neither in whole nor in part, has been previously submitted for any degree.

The work was done under the supervision of Dr. Salman M. Salman from the Physics Department, Alquds University, Palestine and PD Dr. Daniel E. Bürgler from Peter Grünberg Institute, Electronic Properties (PGI-6), Jülich Research Center, Germany.

Mahmoud Zeer

Acknowledgements

First I wish to express my gratitude to the Almighty Allah for providing the grant to make this thesis possible.

Thanks and appreciation to my supervisor Dr. Salman M. Salman who helped me through all stages of my studies and research and established the warm cooperation between Alquds University and FZ-Jülich.

Thanks to my supervisor Dr. Daniel E. Bürgler from PGI-6 FZ-Jülich centre for his support and encouragement and for providing the opportunity to acquire the knowledge in this field of research. My gratitude also goes to Dr. Frank Matthes, Volkmar Hess and the FZ-Jülich staff for their moral and spiritual support.

Many thanks to my family and friends, who stood beside me and encouraged me constantly.

Mahmoud Zeer

This project is the first of a collaborative effort under the SCP-1 part of the framework collaboration between Jülich Research Center, Germany, and Alquds University, Palestine, and coordinated by Professors Claus Schneider the head of Peter Grünberg Institute, Electronic Properties (PGI-6) and Salman M Salman from Alquds Physics department, director of Alquds side of Jülich-Alquds Cooperation. The research was thankfully funded by PGI-6.



Abstract

In the course of this thesis, the capability of adsorption by the double-cuboid Polyoxopalladates (**POP**) molecules on the conductive surfaces of Au (111) and HOPG has been investigated, for a potential application in future spintronics devices as precursors. Deposition was carried out by the drop casting method, where a droplet of solution is applied onto the substrate and left to evaporate for 1 hour under ambient conditions. *In-situ* experimental techniques for the characterization of POP adsorption, such as Auger Electron Spectroscopy AES, and Scanning Tunneling Microscopy STM techniques have been used. The results demonstrated by AES show the capability of POP molecules to adsorb on the chosen substrates.

Imaging of the POP molecules by STM was successfully conducted. The measured width of some lines structures POP molecules was largely compared to the molecules size on the Au (111) surface at low concentration. Aggregation of molecules should depend on the intermolecular and molecule-surface interactions but a clear explanation for the specific structure needs further measurements.

Depositing POP molecules on HOPG was generally successful. Imaging of intact molecules with different orientations and various arrangements in ordered arrays and chains was achieved with high topographic resolution in some of the cases. The arrays followed the surface structure but the chains were specifically located along the arrays edges.

Further research is needed to obtain a detailed understanding of the various configurations and to explain the anomalies. STM Measurements for lower concentrations and a detailed investigation of the depositions by AES are suggested. Few more recommendations for measurements to study other aspects for possible applications are proposed.

Polyoxopalladates on Au (111) and HOPG Substrats

Content	Page
Abstract	iii
List of Figures	vii
Abbreviations	xi
Chapter 1: Introduction	
1.1 About the Research Center Jülich.....	1
1.2 General Overview and Motivation of the Research.....	2
Chapter 2: Experimental Techniques	7
2.1 Scanning Tunneling Microscopy (STM).....	7
2.1.1 Principle.....	7
2.1.2 The electron tunneling effect	8
2.1.3 STM imaging modes operation.....	9
2.1.4 Components of STM	10
2.2 Low-Energy Electron Diffraction (LEED).....	12
2.3 Auger Electron Spectroscopy (AES).....	15
2.4 The Ultra-High Vacuum system (UHV).....	17
2.4.1 The Preparation chamber	18
2.4.2 The Molecule deposition chamber	19
2.4.3 The STM Chamber	19
Chapter 3: Experimental Procedures	20
3.1 The POP Molecules.....	20
3.1.1 Synthesis and structure of POP molecule.....	20
3.1.2 The POP properties.....	21

3.2 The Substrate preparation.....	22
3.2.1 Gold (111).....	22
3.2.2 Highly oriented pyrolytic graphite (HOPG).....	25
3.3 Drop Casting Method.....	27
3.4 Tungsten Tip Preparation.....	28
Chapter 4: Results and Discussion	29
4.1 Experimental Conditions	31
4.2 AES of POPs adsorbed on Au (111) and HOPG substrates	32
4.3 POP molecules on The Au (111) substrate	33
4.4 POP molecules on HOPG substrate.....	36
4.4.1 Well-ordered of POPs lines on the HOPG surface.....	36
4.4.2 Observation of molecular chains and arrays on HOPG.....	38
4.4.3 Molecule arrays comparison	41
4.4.4 Molecule array structure as a function of tunneling current	42
4.4.5 Molecule array profile dependence on bias voltage	43
4.4.6 Double layers of the molecular arrays	44
Chapter 5: Conclusions and Summary	46
Bibliography	50

List of Figures

Figure 1.1 a) Project of synthetic expansion of magnetic molecules into spintronic devices. b) Schematics of future work with POP molecules that could be used as a precursor in spintronics devices. 5

Figure 2.1 Principle of STM and its components. When a negative bias is applied to the sample, the electron tunneling starts from an occupied states of the sample into unoccupied states of the tip. A computer generates the lateral scan motion and records the tunneling current and the piezo feedback signal to form an STM image of the sample. 8

Figure 2.2 One dimensional quantum mechanical tunneling effect. A particle wave Ψ , impinges on an energy barrier of height V_0 and width d . In classical mechanics the wave will be reflected, whereas in a quantum mechanical treatment there is a small but finite probability for the particle to reach to other side of the barrier. i.e. it is said to “ tunnel through the barrier”. 8

Figure 2.3 Constant- height and constant-current operation modes of STM. 10

Figure 2.4 Left: Schematics of the translation between the real and reciprocal spaces. Right: Construction of the Ewalds sphere for the case of diffraction from 2D-lattice. The intersection between the Ewalds sphere and reciprocal lattice rods define the allowed diffraction beam. 13

Figure 2.5 LEED optics produced by Omicron, viewed from the vacuum side. The top shows the grids that filter the in-elastically scattered electrons. Below the stack of the grids the fluorescent screen is hidden. The electron gun is aligned vertically and penetrates through the center of the grids, pointing towards the sample (not shown), which must be placed in grids center of curvature and the screen. 14

Figure 2.6 Schematic diagram of a typical LEED experiment. The electron gun produces a mono-energetic beam, the hemispherical grid system repels electrons having energies below the elastic energy (i.e. the acceleration energy of the gun),

and the diffracted electrons are then accelerated toward the fluorescent screen, where they produce the LEED pattern. 15

Figure 2.7 Schematic diagrams for the photoemission (middle) and Auger (right) process. Labels V, M, L₂₃, L₁, and K represent the electron orbits. 16

Figure 2.8 Photograph showing a part of the experimental setup: (1) Load-lock chamber, (2) SEM chamber, (3) preparation chamber, (4) STM chamber, (5) molecule evaporator, (6) manipulator, (7) transfer rods, and (8) separation valve. 18

Figure 3.1 Four different concentrations (ranging from 10⁻⁵ to 10⁻⁸ molar) of POPs dissolved in H₂O. 21

Figure 3.2 Ball-and-stick/polyhedral representation of Na₂₀[Cu₂Pd^{II}₂₂P₁₂O₆₀(OH)₈].58H₂O. Color code: Cu (turquoise), Pd (blue), O red balls, {PO₄} tetrahedral (purple). The very long Cu-O bonds [2.759(6) – 2.839(6) Å] are indicated by dotted lines. 22

Figure 3.3 Auger spectrum of the Au (111) surface after the cleaning process indicating a clean surface. No other chemical elements can be detected. In particular, no carbon (275 eV) and oxygen (510 eV) can be observed indicating a clean surface. 24

Figure 3.4 LEED pattern of the Au(111) surface (electron energy = 119.9 eV). 25

Figure 3.5 (a-c): a) Atomic resolution of the Au(111) surface. Area 3 nm × 3 nm, I_T = 0.8 nA, U_{gap} = 0.5 V at 77 K. b) line section along the white line in a). c) STM image of the herringbone reconstruction of Au(111). I_T = 0.5 nA, U_{gap} = 0.32 V at 77 K. 25

Figure 3.6 Top (a) and side (b) view of the HOPG structure. 27

Figure 3.7 LEED pattern of the HOPG surface (with electron energy 92.3 eV). 27

Figure 3.8 Auger spectrum of the HOPG surface after the cleaning process. The blue arrow indicates the main peak of carbon (275 eV). 28

Figure 3.9 Atomically resolved STM imaging of the HOPG surface. $4 \text{ nm} \times 4 \text{ nm}$, $I_T = 0.2 \text{ nA}$, $U_{\text{gap}} = 0.5 \text{ V}$ at 77 K . (b) Line section along the white line in (a). 29

Figure 3.10 Setup of the electrochemical etching of the W-tips. The etching takes place at the small region around the W-wire that is immersed in the caustic soda solution (NaOH) and is not protected by the plastic tubes. 30

Figure 4.1 (a) Auger spectrum after deposition POPs from different solutions onto Au(111) substrates. 32

Figure 4.1 (b) Auger spectra before and after deposition of 10^{-7} molar of POP solution onto HOPG surfaces. 33

Figure 4.2 Auger spectra of the Au (111) substrate after expose to air (a), and to the solvent only (b). 34

Figure 4.3 (a) STM image after exposure of the Au(111) surface the to air showing terraces. The $200 \times 200 \text{ nm}$ image is taken at $I_T = 1 \text{ nA}$, $U_{\text{gap}} = 0.5 \text{ V}$. (b) STM image of the Au(111) surface after depositing the solvent (H_2O) only. The $50 \times 50 \text{ nm}$ image is taken at $I_T = 1 \text{ nA}$, $U_{\text{gap}} = 1 \text{ V}$ at RT. 34

Figure 4.4 (a) STM image of a line structure on Au (111) after adsorbing POP molecules from an aqueous solution. Terraces and some contamination are visible on the right side; Area = $200 \text{ nm} \times 200 \text{ nm}$, $I_T = 0.15 \text{ nA}$, $U_{\text{gap}} = -0.55 \text{ V}$. (b) Line section along the white line in (a). (c) Zooming into a part of the line in (a) showing the herringbone structure of the Au (111) substrate (in the parts of the terrace on the right) and the line with better resolution. (d) Selected rectangular in (c) in order to show the contrasts inside the line structure. (e) Line section along white line in (d). 35

Figure 4.5 (a) STM image of double-cuboid-shaped POP molecules on the HOPG surface, area $32.2 \text{ nm} \times 22.1 \text{ nm}$, $I_T = 1.5 \text{ nA}$ and $U_{\text{gap}} = 3 \text{ V}$. (b) The molecule height and width are indicated by the line section along the white line. 37

Figure 4.6 STM images of selected sections of a 430 nm long molecule chain. (a) Upper end of the chain, (b) middle part, and (c) lower part of the chain also showing HOPG steps. The 125 nm × 125 nm images are taken at $I_T = 1.5$ nA and $U_{\text{gap}} = -0.5$ V. 37

Figure 4.7 STM image taken with $I_T = 1.5$ nA, $U_{\text{gap}} = -0.1$ V, and scan area 46.3×46.3 nm² showing a molecular chain crossing HOPG steps (a) and a cross section of the substrate step revealing its monatomic height (b). 38

Figure 4.8 (a) STM images of large scan-area of POP showing both a molecule chain and a molecular array on HOPG. (b) A selection from (a) showing better resolution especially for the molecule array. (area (a) = 180 nm × 180 nm, (b) = 66.6 nm × 66.6 nm), $I_T = 1.5$ nA and $U_{\text{gap}} = 3$ V. 38

Figure 4.9 large scan areas STM image for POPs covering a HOPG surface. The POP array extends from the molecule chain at the bottom up the top of the image. Scan area 200 nm × 200 nm, $I_T = 1.5$ nA and $U_{\text{gap}} = 3$ V. 39

Figure 4.10 STM images of molecule arrays on HOPG. Scan area 20 nm × 20 nm, $I_T = 1.5$ nA and $U_{\text{gap}} = 1$ V. 40

Figure 4.11 (a) High resolution STM topography of a densely packed POP molecule arrays on HOPG surface with the unit cell of the superstructure as indicated by the red lines with hexagon shape with one molecule at the center (area = 17.3 nm × 9.8 nm, $I_T = 1.5$ nA and $U_{\text{gap}} = 3$ V). (b) A cross section along the white line in (a). (c) STM image of molecule arrays with different geometries (area = 11.1 nm × 11.1 nm, $I_T = 1.5$ nA and $U_{\text{gap}} = 3$ V). (d) A cross section along the white line in (c). 41

Figure. 4.12 Constant current STM images of molecular arrays of POPs on the HOPG surfaces as a function of tunneling current. Tunneling current in (a) 1.5 nA, (b) 1 nA, (c) 0.5 nA and (d) 0.3 nA. [(a) – (d) size area = 20 nm × 10 nm and $U_{\text{gap}} = -0.5$ V]. 42

Fig 4.13 Constant-current STM images of POP molecules on the HOPG surface as a function of the bias voltage. Bias voltage (a) 1.5 V, (b) 2 V, (c) 3 V, (d) -0.1 V, (e) -0.3 V, (f) -2 V. [(a) – (f) image area $6.67 \text{ nm} \times 6.67 \text{ nm}$ and $I_T=1.5 \text{ nA}$]. 44

Figure 4.14 (a) Constant-current STM topography of a POP molecule array on the HOPG surface showing a non-uniform lattice with a dislocation (blue circle). (b) Line section along white line in (a). Image size $20 \text{ nm} \times 20 \text{ nm}$, $I_T = 1.5 \text{ nA}$ and $U_{\text{gap}} = 1 \text{ V}$. 45

Abbreviations

AES	Auger Electron Spectroscopy
DOS	Density Of State
FCC	Face Centered Cubic
HOMO	Highest Occupied Molecular Orbital
HOPG	Highly Oriented Pyrolytic Graphite
LDOS	Local Density Of State
LEED	Low Energy Electron Diffraction
LUMO	Lowest Unoccupied Molecular Orbital
POP	PlyOxoPalladates
POM	PolyOxoMetalates
RT	Room Temperature
STM	Scanning Tunneling Microscope
UHV	Ultra-High Vacuum

Chapter 1

Introduction

1.1 About the Research Center Jülich

The experimental work presented in this thesis was performed at the Research Center Jülich in Germany.

The Research Center Jülich (FZJ) is a member of the Helmholtz Association, and one of the major research institutions in Europe. Key technologies in the areas of health, environment, and information characterize the profile of the Forschungszentrum Jülich.

The potential of the FZJ for meeting the objective of "key technologies for tomorrow" lies in 4,600 employees who work together in an interdisciplinary manner, over 200 cooperation partners in Germany and abroad, a unique infrastructure, and a special expertise in physics, materials science, nanotechnology, and information technology.

The Forschungszentrum Jülich is proud of the tools it provides for its researchers to do their work: simulation with supercomputers, research with neutrons, imaging techniques for medicine, nanotechnology tools. These modern instruments allow science to break through to new horizons of knowledge. This infrastructure, valued and used by researchers throughout the globe, characterizes Jülich as the home of key technologies.

The Research Centre is located near the town of Jülich, close to the university cities Aachen, Bonn, Cologne and Düsseldorf. The proximity of Jülich to the Netherlands, Belgium and Luxemburg as well as about 700 international guest scientists per year adds to an excellent and inspiring training environment.



1.2 General Overview and Motivation of the Research

Nanotechnology describes science and technology that create, control, and take advantage of material structures with characteristic dimensions in the range of less than 100 nm. The long-term aim of this technology is to design materials devices with specific and advanced features by controlling processes at the ultimate length scale of atoms and molecules [**Whitesides and love, 2001**].

To achieve these aims, fundamental issues have to be addressed in areas as varied as molecular biology, catalysis, lithography, and molecular scale devices [**Balzani et al. 2000**]. Nanotechnology emanates from the demand to explore alternatives to the traditional “top-down” approach in semiconductor industries that uses lithography techniques for the fabrication of smaller and smaller electronic components on silicon wafers.

In 1965, Moore predicted that the number of transistors per integrated circuit (IC) would double every 18 months [**Moore, 1965**]. The downscaling of the optical lithographic process is curial due to both fabrication costs and reaching the fundamental physical limits [**ITRS, 2001**] and [**Special issues, 2000**].

A revolution in electronics is going on with the contemporary development of two novel disciplines, namely spintronics and molecular electronics. Magnetic molecules form a link between the two fields. They offer unique properties such as metallic or semi conducting behavior, high magnetic moments, size-inducing quantum effects, and a manifold of functions leading to electric, magnetic, optical, and chemical sensitivities or selective reactions with their environment. The resulting research field, Molecular Spintronics, aims at manipulating spins and charges in electronic devices containing one or more molecules [**Bongani and Wernsdoefer, 2008**], [**Cleuziou et al. 2006**], and [**Roch et al. 2008**].

Great attention is paid to spintronics systems where the electronic charge and spin degrees of freedom can be used simultaneously in order to produce devices with new functionality for an emerging technology. In the last ten years some fundamental results turned into actual devices. Therefore, molecular spintronics holds great promises for the future.

Spintronics take advantage of the fact that the electronic current is composed of spin-up and spin-down carriers that carry information encoded in their spin state and interact differently with magnetic materials. Information encoded in the spins persists when the device is switched off. It can also be manipulated with and without using external magnetic fields and can be written using little energy [Wolf et al. 2001] and [Awschalom and FLatt, 2007].

Devices employed in molecular electronics are most often composed of two nano-electrodes and a bridging molecule in between, allowing the measurement of electron transport through a single molecule, and the measurement is carried out at the molecular level. The observables are connected to molecular orbitals rather than to Bloch waves in bulk materials. [Chiang et al.1994]

Consequently, quantum properties of the molecule can be probed directly using new rules governing these systems. The roles include electron tunneling processes in the electrode-molecule-electrode system that can exhibit the presence of Kondo or Coulomb-blockade effects, taking into account the binding strength between the molecule and electrodes that can be tuned by selecting the appropriated chemical functional groups [Bogani and Wernsdorfer, 2008].

Currently, different aspects have been studied, such as singly adsorbed molecules [Thomas et al. 2001], monolayer structures [Chen et al. 2002] and [Lukas et al. 2002] and thin film growth [Meyer et al. 2001] using the powerful STM techniques for atomic scale studies. The study of organic molecules on surfaces started after the invention of the STM [Cui et al. 2001] and [Nanoelectronics, 2005], and quite soon it was extended to large and complex molecules due to their prospective applications in nano-electronics, molecular devices and spintronics. Important insight into the bonding and ordering of molecules on different substrates has been gained.

The investigation of functional molecules on solid substrates is increasingly becoming a crucial aspect of Nanoscience, especially in molecular and supramolecular electronics and spintronics. In this respect molecular electronics and spintronics emerge as competitive alternatives to conventional top-down approaches to reduce size and the cost per functional unit. The synthesis

of molecules allows tuning typical properties that contribute to the suitability for the integration into electronic devices. Examples are the coupling to electrodes, the magnetism, or the transport properties. **[Ishikawa et al. 2004]**.

Recent years have seen increased interest in imaging individual molecules adsorbed on substrates by the STM techniques. Molecules forming insulating substances in their bulk structure have successfully been imaged by deposition them on conductive substrates **[Chiang et al. 1994]**, **[Jung et al. 1998]** and **[Fisher and Blochl, 1993]**. This is surprising since for insulating molecules the energy gap between the highest occupied molecular orbital (HOMO) and lowest unoccupied molecular orbital (LUMO) is relatively large **[Song et al. 2002]**. The main explanation is the decrease of the HOMO-LUMO energy gap due to intermolecular or molecule-substrate interactions. Some years ago several groups have reported STM images for ordered monolayer arrays of Polyoxometalates (POMs) on different substrates **[Song et al. 2002 and 2003]** and **[Kaba et al. 1998 and 2002]**.

Although STM is capable of atomic resolution when imaging solid surfaces, mapping of large and complex molecules with sub-molecular resolution is a difficult challenge. In particular at ambient condition, merely mapping the Van der Waals surface of often very dense molecules assemblies would only provide a featureless “blob” for a large cluster of atoms. However, STM images taken under well-defined conditions (such as UHV, low temperatures, and clean contamination-free surfaces) contain both geometric and electronic information about the sample. Therefore, highly resolved STM images can differentiate between molecules adsorbed on surfaces with very similar geometric structures **[Errington et al. 2005]**, **[Feyter and Schryver, 2005]** **[Hembacher et al. 2005]**.

Polyoxometalates (POM) are usually formed by group 5 and 6 metals in high oxidation states (e.g., V^{5+} , Nb^{5+} , Mo^{6+} , Ta^{5+} , and W^{6+}) **[Barsukova-Stuckart et al. 2012]**. Recently however, several “unconventional” noble metal-oxygen clusters based on Pt^{2+} , Pd^{2+} , and Au^{3+} have redefined our understandings. They can be considered intermediate between metal ions and extended metal-oxide lattices. In fact, polyanions are frequently referred to as “molecular metal-

oxide fragments". Some polyanion derivatives have the potential to become crucial building blocks of solid-state electronic, magnetic and optical devices in modern technology. [**Nano molecular science**]

Recent progress in polyoxometalate chemistry has allowed the design of polyoxomolybdates, polyoxotungstates, and polyoxopaladates with multiple functionalities and dimensions in the nano-regime. This class of molecular compounds is expected to play an important role in the rapidly expanding field of Nanoscience and nanotechnology. Rational synthesis of polyoxometalates usually follows a self-assembly mechanism involving lacunary precursors. In the final product, the polyanion, vacant subunits can incorporate the functionalities appropriate for the construction of miniaturized molecular devices. [**Nano molecular science**]

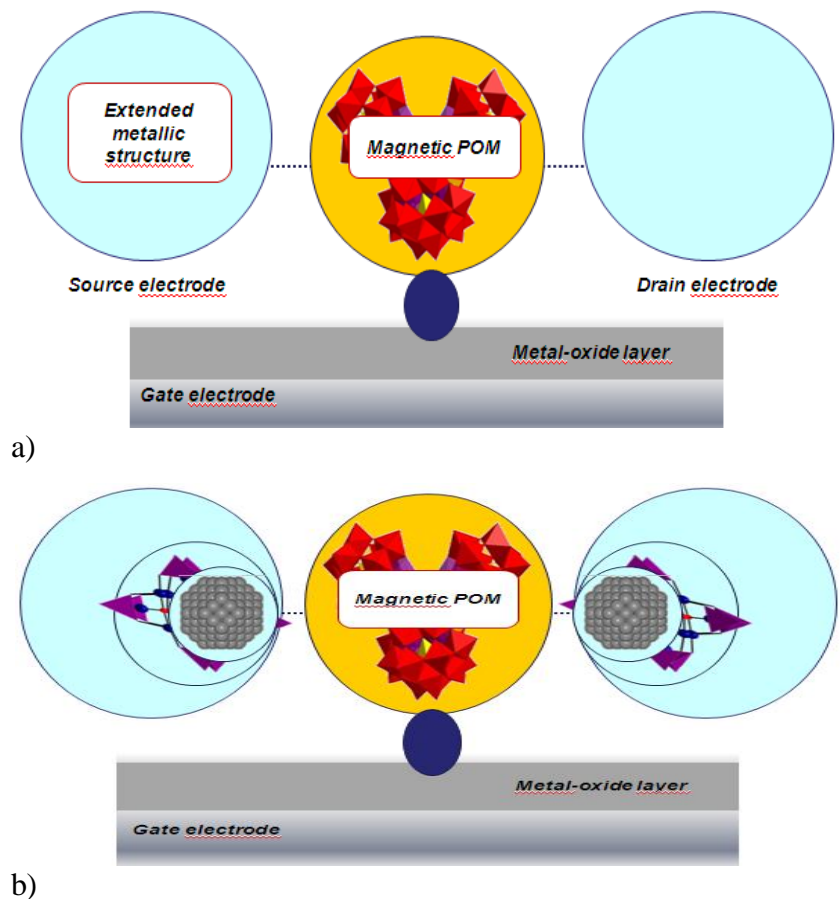


Figure 1.1 a) Project of synthetic expansion of magnetic molecules into spintronic devices. b) Schematics of future work with POP molecules that could be used as a precursor in spintronics devices. [**Courtesy of Prof. Paul Kögerler, RWTH Aachen and FZJ**].

The research presented in this thesis concentrates on the adsorption characteristics of double-cuboids-shaped insulating Polyoxopalladates molecules $\text{Cu}_2\text{Pd}_{22}\text{P}_{12}\text{O}_{60}(\text{OH})_8]^{20-}$ (**POP**) on two differently reactive surfaces, namely Au(111) and HOPG using AES and STM. This molecule is a promising candidate as a precursor for fabrication advances as suggested in Figure 1.1. To my knowledge, there are no previous reports of STM studies for these molecules.

The surface characterization before depositing the POP molecules onto Au (111) and HOPG substrates was performed by surface-sensitive AES, low-energy electron diffraction (LEED), and STM. Combining the results obtained from these techniques makes it possible to get atomic scale information regarding the geometric structure of the system, the chemical composition, and the molecule-substrate interactions, which are key aspects of the research work presented here.

This thesis is composed of five chapters. This chapter presents a brief introduction to the project background. In chapter two we describe the experimental techniques, Chapter three deals with the experimental setup and sample preparation that includes the structure, synthesis and properties of POP and the experimental procedures, respectively. The results and analyses are discussed in some detail in chapter four. Summary and conclusions and recommendations are presented in chapter five.

Chapter 2

Experimental Techniques

This chapter is devoted to review the experimental techniques utilized for this work. A brief review of the STM principle, LEED, and AES used for surface investigation is presented. Finally an introduction to the ultra-high vacuum system and its main chambers is given.

2.1 Scanning Tunneling Microscopy (STM)

The direct investigation of the sample surface and its adsorbates was done in this work using STM. A commercial low-temperature STM by Omicron was used to obtain the measurements.

2.1.1 Principle

In 1986 Gerd Binnig and Heinrich Rohrer were awarded the Noble prize in physics for the invention of the scanning tunneling microscope in 1982. STM is a technique capable of directly imaging not only the surface and its adsorbates, but also the electronic and spin-polarization properties of single molecules [Binnig and Rohrer, 2000] and [Binnig and Rohrer, 1986]. STM uses the quantum-mechanical electron tunneling through a barrier between two conductors.

The basic principle of operation of STM is to move a sharp metallic tip within a distance of few Å from a surface. In this configuration the tip and the surface electronic wave functions overlap. When we apply a voltage of up to a few volts between the tip and the surface, the electrons tunnel from the surface to the tip or vice versa, depending on the polarity of the voltage as shown in Figure 2.1. Tunneling electrons produce a small current (few pA to- μ A), called the tunneling current I_T , that depends exponentially on the spacing between tip and surface.

This is the key to the high vertical resolution. The vertical position of the tip is controlled by a piezo actuator, which also scans the tip across the surface to be imaged. The current I_T (constant-height mode) or the piezo voltage required to keep I_T constant (constant-current mode) are recorded by a computer and when plotted over the scan positions they form the STM image of the surface.

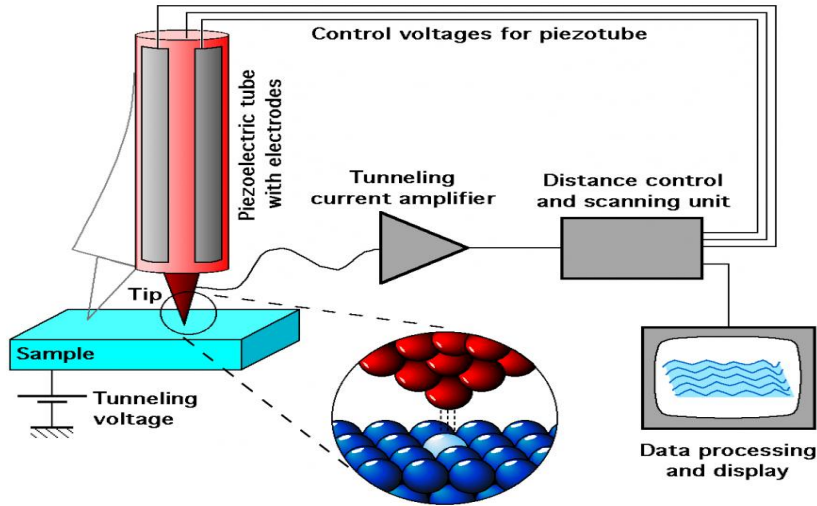


Figure 2.1 Principle of STM and its components. When a negative bias is applied to the sample, the electron tunneling starts from occupied states of the sample into unoccupied states of the tip. A computer generates the lateral scan motion and records the tunneling current and the piezo feedback signal to form an STM image of the sample [IAP, 2012].

2.1.2 The Electron Tunneling Effect

The quantum mechanical tunneling process in one dimension can demonstrate the concept of STM imaging [Bonnell, 2001]. Figure 2.2 shows the state of a particle described by the wave function ψ that tends to cross an energy barrier of height V_0 that is extending from 0 to d along the z axis.

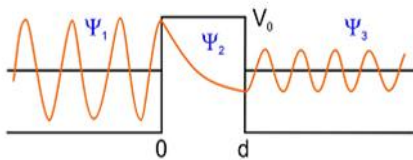


Figure 2.2 One dimensional quantum mechanical tunneling effect. A particle wave ψ_1 impinges on an energy barrier of height V_0 and width d . In classical mechanics the wave will be reflected, whereas quantum mechanics allows for a small but finite probability of transmission or tunneling to other side of the barrier [Bonnell, 2001].

Solving the time-independent Schrödinger equation

$$\frac{-\hbar^2 d^2 \psi(z)}{2m dz^2} + V(z)\psi(z) = E \psi(z) \quad 2.1$$

one can determine the transmission or tunneling probability. Here m and, \hbar are the mass of the electron and the reduced Plank's constant. It is helpful to divide the z axis into three regions as

sketched in the Figure 2.2. In regions I and III the sample potential $V(z) = 0$, whereas in region II $V(z) = V_0$. The electron wave functions for these regions have the form

$$\psi(z) = \begin{cases} Ae^{iKz} + Be^{-iKz}, & z < 0; \\ Ce^{kz} + De^{-kz}, & 0 \leq z \leq d; \\ Ee^{iKz}, & z > d \end{cases} \quad 2.2$$

where $K = \frac{2m}{\hbar^2}\sqrt{E}$ and $k = \frac{2m}{\hbar^2}\sqrt{E - V}$. The coefficients A, B, C, D, and E are determined from the boundary conditions at $z=0$ and $z=d$, which require the continuity of wave functions and their derivatives. The tunneling current is directly connected to the transmission probability T or coefficient that is defined as the ratio between intensities of the transmitted $|C|^2$ and incoming $|A|^2$ waves.

$$T = \frac{|C|^2}{|A|^2} \quad 2.3$$

Taking into account a thick and high potential barrier $kd \ll 1$, a typical condition for the STM, we can approximate T as

$$T \approx \frac{16 K^2 k^2}{(K^2 + k^2)^2} \cdot e^{-2kd}. \quad 2.4$$

This is the basis for estimating the STM current. It shows very high dependence and sensitivity towards the effective barrier height and thickness. For typical STM experiments the barrier height is about 4 eV and the width is few angstroms. The transmission current is very sensitive to the variation in these parameters. A variation of the barrier width by 1\AA changes the tunneling current by almost one order of magnitude.

2.1.3 STM Imaging Mode Operations [Besenbacher, 1986]

STM offers two basic modes of scanning: constant-current mode, and constant-height mode. In the constant-height mode, the tip is scanned across the surface at a constant average height. Thereby, the tunneling current varies according to the local distance between the tip and the surface. Tiny changes of this distance, e.g. due to atomic scale corrugation, translates according Eq. 2.4 into measurable variation of the tunneling current.

The topographic image acquired in this mode is represented by plotting the tunneling current as a function of lateral tip position. This mode is only adequate for flat surfaces and small scan areas, typically $5 \times 5 \text{ nm}^2$.

Alternatively, in the constant-current mode the tip scans the xy -plane, while the height z is adjusted by a feedback system to maintain a constant tunneling current. This is achieved by changing the voltage on the z -piezo element. The image is formed by plotting the z -piezo feedback voltage as a function of the scan position. Generally, the constant-current mode yields better resolution and it also works with atomically not flat (e.g. stepped) surfaces, but has the disadvantage of lower scanning speed. All images taken in this work were obtained in the constant-current mode. The two images modes are depicted in Figure 2.3.

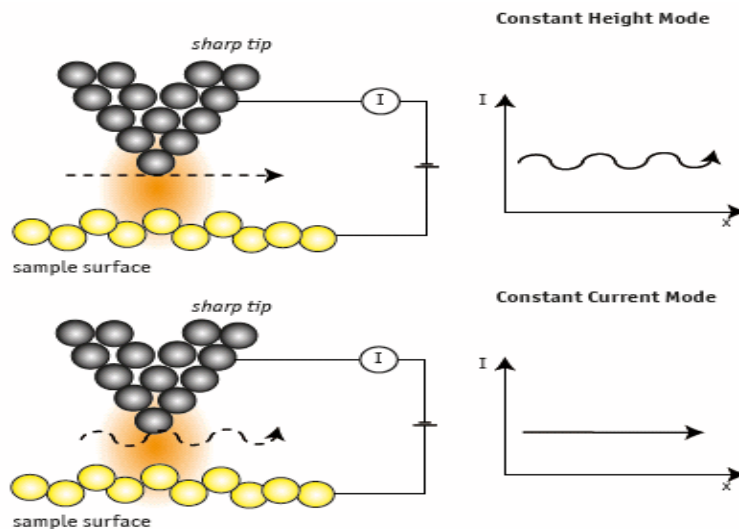


Figure 2.3 Constant-height and constant-current operation modes of STM [Attocube].

2.1.4 Components of STM

In our experiment we used the low-temperature Omicron STM at the Nanospintronics cluster tool (NCST) of the Peter Grünberg institute at the Forschungszentrum Jülich. The instrument is equipped with liquid Helium cooling and the lowest temperature that can be achieved is around 4.7 K. Tungsten tips installed into a cylindrical piezo element are used to perform the STM measurements.

The movement of the tip along the z direction is controlled by piezo-driven stick-and-slip linear stepper motors. The coarse motion is manually operated while the tip-sample separation is monitored by a CCD camera. After the mirror image of the tip on the sample surface and direct image of the tip are close enough, the auto-approach procedure is started. A computer generated linear voltage ramp is applied to the z-piezo in order to move the tip to the closest distance to the sample. If tunneling current is detected during this motion, the feedback-loop is activated and the auto-approach stops. If the tip does not reach the tunneling regime, it is fully retracted and a single step of the coarse stepper motor moves the tip and the scanning piezo closer to the surface. The next cycle of the auto-approach is started by again applying the linear voltage ramp to the z-piezo.

The cycle is automatically repeated until the set-point tunneling current defined by the user is detected. Then, we can scan the surface by moving the piezo scanner in x- and y-directions. Topographic data based on the z-position is collected by the STM computer. Both forward and backward scan images were recorded.

A key part of the STM instrument is the piezoelectric material, which has the ability to contract and expand when an electric field is applied. The STM piezoelectric element contracts or expands by 0.01 \AA/mV , and that allows for angstrom-level fine control of the tip head [**G. Binnig and H. Rohrer, 2000**].

STM instruments need to be isolated from external vibrations to avoid mechanical instabilities of the tip-surface gap. Vibrational damping of the instrument is used to achieve sub-angstrom precision in both lateral and vertical tip positioning. For this purpose our STM employs a spring systems with eddy current damping.

In principle, STM operation does not require vacuum and can be used under different pressures ranging from the atmospheric down to ultra-high vacuum pressure, an environment needed to avoid contamination or oxidation of the sample, that both have severe impact on the tunneling current and thus the quality images.

2.2 Low-Energy Electron Diffraction (LEED)

The preparation chamber provides an Omicron spectra LEED, consisting of an electron gun and an analyzer screen. LEED is a technique, which is widely used to characterize the structure of surfaces [Diehl et al. 2003] in surface science laboratories because of the relatively low cost, compactness, and ease of performance in the UHV [Seah and Dench, 1979]. The usage of low-energy electrons for surface analysis emanates from the following reasons.

1- The de-Broglie wavelength of electrons is given by

$$\lambda = \frac{h}{\sqrt{2mE}}, \quad \lambda [\text{\AA}] = \sqrt{\frac{150}{E(\text{eV})}} \quad 2.5$$

For electrons with an energy E of 20-200 eV, λ is of the order of 1-2 Å and is thus suitable to resolve atomic structures in a diffraction experiment.

2- The mean free path of the low-energy electrons in solids is very short. Therefore, most elastic collisions occur in the very few topmost layers of the sample in the diffraction process [Oura, 2003]. Whence LEED provides information mostly about the surface atomic structure.

For the case of the diffraction on the 2D surface, the crystal periodicity in the direction normal to the surface is lacking and the condition for constructive interference and hence diffraction of scattered electron wave is given by the Laue condition in two dimensions

$$\mathbf{k}^{\parallel} - \mathbf{k}_0^{\parallel} = \mathbf{G}_{hk} \quad 2.6$$

where, \mathbf{k}_0 , \mathbf{k} are the incident and scattered wave vectors respectively, and \mathbf{G}_{hk} is the reciprocal lattice vector in the sample plane.

Conservation of momentum concerns only the wave vector components parallel to the surface. The scattering vector component parallel to the surface, $(\mathbf{k}^{\parallel} - \mathbf{k}_0^{\parallel})$, must be equal to the vector of the 2D surface reciprocal lattice, \mathbf{G}_{hk} . In elastic diffraction collisions both energy and momentum are conserved, whereas the direction of momentum is changed.

The Laue condition in the 2-D reciprocal space and the Ewald sphere can be used to describe the whole LEED process. Equation 2.7 shows the way to construct the 2-D reciprocal space.

$$\vec{a}^* = 2\pi \cdot \frac{\vec{b} \times \vec{n}}{|\vec{a} \times \vec{b}|} \quad \vec{b}^* = 2\pi \cdot \frac{\vec{n} \times \vec{a}}{|\vec{a} \times \vec{b}|} \quad 2.7$$

where \vec{a}^* and \vec{b}^* are the reciprocal lattice vectors of the surface lattice spanned in real space by the lattice vectors \vec{a} and \vec{b} . The constant \vec{n} is a unit vector normal to the surface plane. The Laue condition can readily be visualized using the Ewald's sphere construction. Figure 2.4 shows a simple illustration of this principle: The wave vector \vec{k}_o of the incident electron beam is drawn such that it terminates at a reciprocal lattice point O. The Ewald sphere is then the sphere centered at the origin of \vec{k}_o with radius $|\vec{k}_o|$. Obviously, it passes through the reciprocal lattice point O.

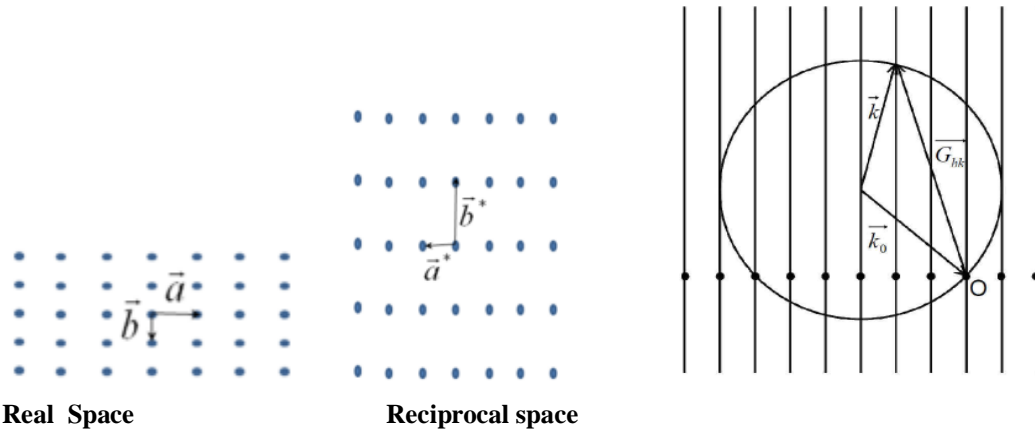


Figure 2.4 left: Schematics of the translation between real and reciprocal spaces. Right: Construction of the Ewald sphere for the case of diffraction from a 2D-lattice. The intersections between the Ewald sphere and reciprocal lattice rods define the allowed diffraction beams [Yan Bai, 2010].

The typical geometry of a LEED experiment is shown in Figures 2.5 and 2.6. The standard set-up for LEED contains the main elements, which are an electron gun, a sample holder, and a hemispherical fluorescent screen. The electron gun provides a nearly mono-energetic beam of electrons with a variable energy in the range from few to some hundreds eV.



Figure 2.5 LEED optics produced by Omicron, viewed from the vacuum side. The top shows the grids that filter the inelastically scattered electrons. Below the stack of the grids the fluorescent screen is hidden. The electron gun is aligned vertically and penetrates through the center of the grids, pointing towards the sample (not shown), which must be placed in grids center of curvature and the screen. [Omicron LEED]

The electrons are accelerated towards the sample in a direction perpendicular to the surface. The back scattered and diffracted electrons are then energy filtered by a retarding field between the grids and form a diffraction pattern on a fluorescent screen located on the same side of the sample as the gun. This pattern of spots contains information about the surface atomic scale structure. In order to generate a clear and unambiguous back-scattered electron diffraction pattern the sample must be a single crystal with a well-ordered surface.

We can consider now the information about the surface structure that can be obtained from the LEED data. First information can be gained from the sharpness of a LEED pattern. The primary inspection of the pattern resides conventionally in the quantitative estimation of the structural perfection of the surface under investigation. The well-ordered surface exhibits a LEED pattern with bright sharp spots and low background intensity, whereas the presence of defects and crystallographic imperfections results in increasing the background intensity and broadening and weakening of the spots. The absence of any spots in the LEED pattern indicates an amorphous, disordered, or finely polycrystalline surface. Second, information can be gained from the LEED spots geometry, by considering the correspondence between the 2D lattice surface and the LEED patterns [Oura, 2003].

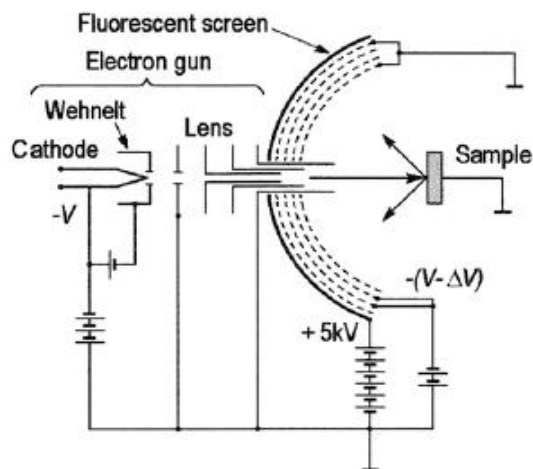


Figure 2.6 Schematic diagram of a typical LEED experiment. The electron gun produces a mono-energetic beam, the hemispherical grid system repels electrons having energies below the elastic energy (i.e. the acceleration energy of the gun), and the diffracted electrons are then accelerated toward the fluorescent screen, where they produce the LEED pattern [Oura, 2003].

2.3 Auger Electron Spectroscopy (AES)

AES is a sensitive technique used for the analysis of the chemical composition of solid surfaces by measuring the energies of Auger electrons [Ertl and Kuppers, 1974], and [Chang, 1971]. Figure 2.7 shows the principle of the Auger process. A primary electron beam of typically (2-10 keV) impinges on the sample and creates a core hole in an inner shells (e.g L_{23} , L_1 or K shells as depicted in Figure 2.7).

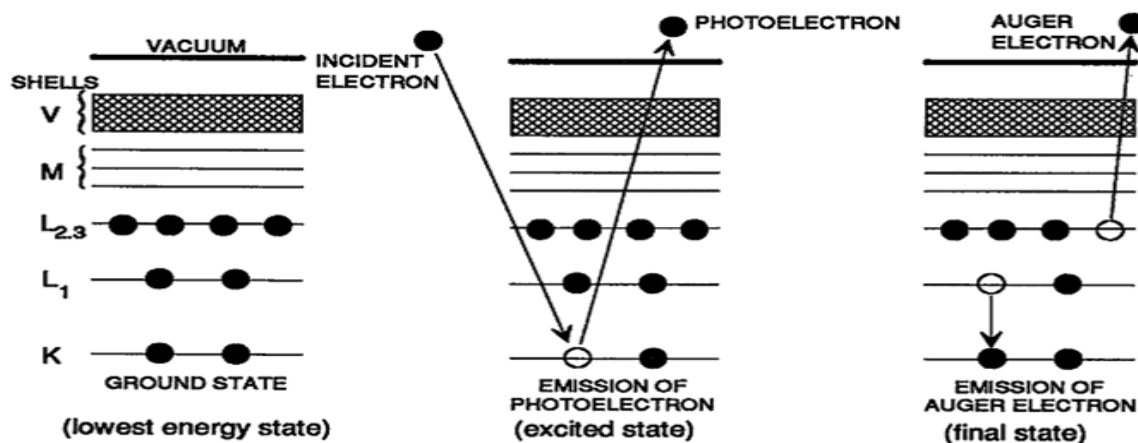


Figure 2.7 Schematic diagrams for the photoemission (middle) and Auger (right) process. Labels V, M, L_{23} , L_1 , and K represent the electron orbits [Nesbitt and Pratt, 1995].

Both the primary and the excited electrons leave the atom. The resultant vacancy can be filled by either a radiative transition (x-ray fluorescence) or a non-radiative transition (Auger emission). In the Auger process an electron from a higher level drops down to fill the core hole, and another electron will be emitted from the ionized atom to stabilize it and conserve energy. That means that three electrons are involved in this process, and thus it can take place for all elements, except H and, He, because they have less than three electrons per atom.

An Auger transition is characterized by the locations of the initial hole and the final two holes. Thus, the energy of the Auger electron in Figure 2.7 is approximately given by

$$E_{KL_1L_{23}} = E_K - E_{L_1} - E_{L_{23}} - \Phi, \quad 2.9$$

where $E_{KL_1L_{23}}$ is the kinetic energy of the Auger electron, E_{L_1} and $E_{L_{23}}$ are the binding energies of the electrons in the L_1 and L_{23} shells, and Φ is the work function of the material. Note that the energy $E_{L_{23}}$ is the binding energy after removal of the core electron from the atom, as the Auger electron emission occurs from the ionized atom, rather than the neutral atom. Using the binding energies of the neutral atom in equation 2.9 is a simplification that is useful for many application of Auger spectroscopy.

A typical Auger spectrometer such as the one used in this work consists of an UHV system, an electron gun for the excitation of the specimen, an electron energy analyzer for the collection of the emitted electrons, and a computer for data storage and processing. Auger analysis is performed in UHV to maintain an uncontaminated surface during the data acquisition [Davis, 1976].

AES is a very surface sensitive technique because the Auger electrons can only travel very short distances through the solid before stopping. Most of Auger electrons will be detected only if they come from the top few atomic layers of the solid. AES can detect very small amounts of elements because even though the probability of exciting an Auger electron of an element is quite high, other de-excitation processes, such as emission of x-rays, will occur.

For chemically simple surfaces, it is relatively easy to get an idea about the elements present. But generally the Auger peaks are rather difficult to detect since they appear in the large tail of the secondary electrons; resulting from a cascade of inelastic collisions between the primary beam electrons and electrons bound in the solid. Experimentally we can improve the detection by differentiating the spectrum with respect to the kinetic energy. Quantitative identification of the elements present on a surface is achieved by comparing the experimental spectrum with Auger transition tables that are available in literature [Davis, 1976]. The lower detection limit for AES is of the order 1% [Zangwill, 1988].

2.4 The Ultra-High Vacuum System (UHV)

The UHV inside the chambers is achieved by using different pumping stages. To reduce the pressure from ambient to 10^{-3} mbar a rotary pump is used. Afterwards turbo molecular pumps (TMP) are switched on to pump the system further down. After baking the system at a temperature of 100°-200°C (depending on the maximum allowed baking temperature) for 48 hours the pressure reaches the order of 10^{-9} mbar.

After cooling the system to room temperature all components of the setup (e.g. filaments) in the UHV are degassed. Finally, a base pressure of 10^{-11} mbar is achieved by ion getter pumps in combination with titanium sublimation pumps. The rotary pumps were located separately in a room next to our system to avoid mechanical vibrations during the high-resolution measurements. The TMP can also be switch off for this purpose.

The UHV system consists of five chambers, namely the load-lock, the molecular deposition, the preparation, the scanning electron microscopy (SEM), and the STM chambers. All chambers can be separated from each other by valves.

The chambers and most of the in-situ parts are made of stainless steel, which is a suitable vacuum material due to its low gas permeability, resistance to corrosion, and possibility to manufacture the internal surfaces with high polish to reduce the surface adsorption. Figure 3.4

shows a photograph of the UHV system called **Nanospintronics Cluster Tool**. In the following a brief description of the instrumentation relevant to this work is given.

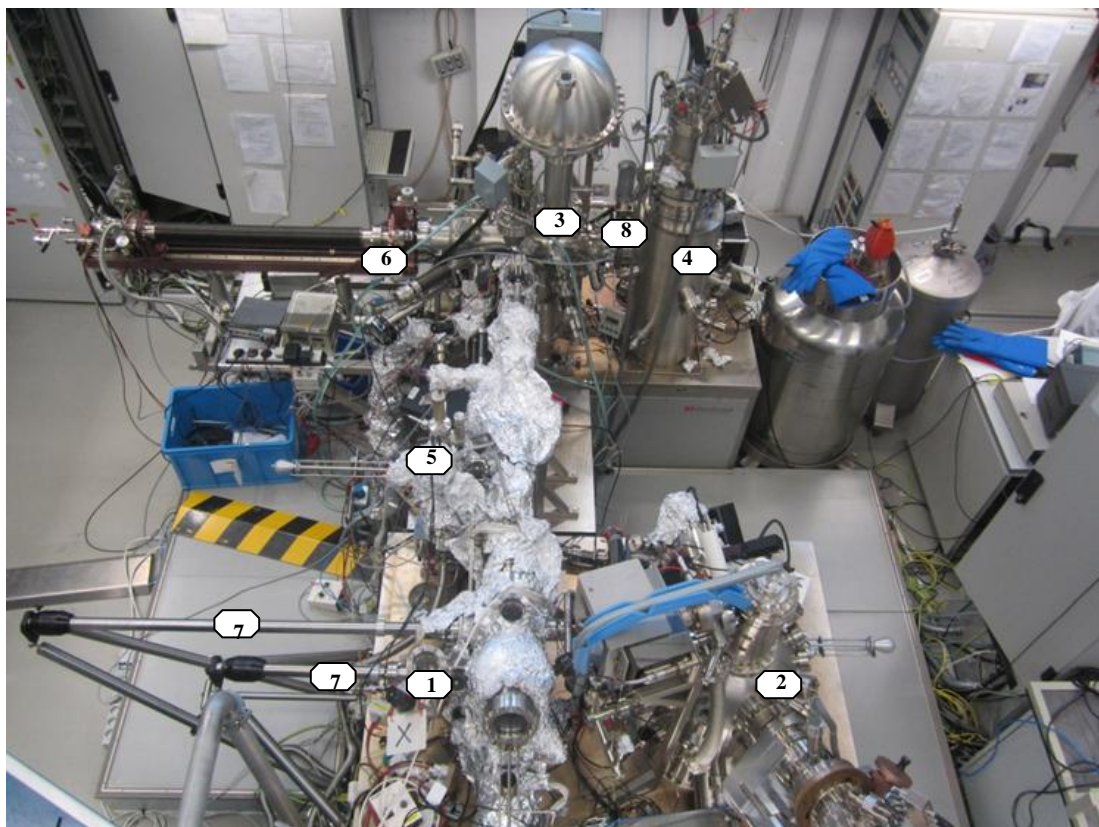


Figure 2.8 Photograph showing a part of the experimental setup: (1) Load-lock chamber, (2) SEM chamber, (3) preparation chamber, (4) STM chamber, (5) molecule evaporator, (6) manipulator, (7) transfer rods, and (8) separation valve.

2.4.1 The Preparation chamber

The main functions of this chamber and its facilities are the preparation and characterization of samples that are used during the work. AES and LEED reveal information about the chemical composition of the surface layers and the atomic structure and symmetry of surfaces, respectively. The chamber is connected with two chambers, (i) the load-lock chamber, from where samples can be introduced to the system, and (ii) to the STM chamber.

Samples and tips are transferred between the chambers via transfer rods. Manipulators, called *wobble sticks*, are used to transfer samples and tips from the transfer rods to the specific equipment such as the STM or heaters. The preparation chamber allows sample heating

(annealing), i.e. warming up and cooling down the crystal at proper temperatures. In order to clean the sample surface, the samples can also be exposed to several cycles of sputtering (i.e. bombardment by an Ar^+ ion beam).

2.4.2 The molecule deposition chamber

The purpose of this chamber is to allow the deposition of molecules by sublimation onto substrates in-situ without breaking the vacuum. The molecule chamber is pumped independently by an additional turbo-molecular pump. It is connected to the preparation chamber and separated by a valve that is opened for few seconds to deposit the molecules. During deposition the pressure worsens for few minutes, and then the base pressure of 10^{-9} mbar can be recovered quickly.

2.4.3 The STM chamber

The STM chamber is connected to the preparation chamber but independently pumped with ion-getter and titanium sublimation pumps. The STM is operated at low temperature to freeze out the mobility of the molecules on the substrate in order to obtain highly resolved topography images and stable conditions for the time consuming STS measurements. Some measurements in this work were performed at 4.8 K achieved by a liquid He bath cryostat.

Chapter 3

Experimental Procedures

This chapter presents an overview of the experimental procedures needed for STM and other measurements of the molecules adsorbed on the surfaces. In section 1 we discuss the POP synthesis and preparation with a brief description of properties that make them a preferable choice. Section 2 provides a description of the preparation of the crystalline substrates. In section 3 a brief description of the method of deposition of molecules onto the clean substrates is presented. Finally, in section 4 we discuss the important experimental issue of the preparation of sharp STM W-tips for the investigation of surfaces at the atomic scale.

3.1 The POP Molecules

We present a brief review of the synthesis and structural characterization of the molecule used in this work. It is the inorganic double-cuboid-shaped polyoxo-22-palladate(II), $[\text{Cu}_2\text{Pd}^{\text{II}}_{22}\text{P}_{12}\text{O}_{60}(\text{OH})_8]^{-20}$ abbreviated as POP molecules or POPs.

3.1.1 Synthesis and structure of the POP molecule

$[\text{Cu}_2\text{Pd}^{\text{II}}_{22}\text{P}_{12}\text{O}_{60}(\text{OH})_8]^{-20}$ was synthesized by the chemistry group at the Peter Grünberg Institute of the FZJ. Dr. Natalya Izarova kindly prepared four different concentrations of POPs for our experiment as shown in Figure 3.1.



Figure 3.1 Four different concentrations (ranging from 10^{-5} to 10^{-8} molar) of POPs dissolved in H_2O .

The molecules were synthesized and characterized using the procedures described in [Barsukova-Stuckart et al, 2011]. H₂O was used as a solvent because the molecules are soluble in water and can be repeatedly recrystallized from aqueous solutions.

3.1.2 The POP Properties

Polyoxopalladates II belong to the noble metal based polyanion family, which is among the water-soluble POM group that has the largest number of members compared to other recently synthesized POM groups [Chubarova et al. 2008], [Izaroya et al. 2009], and [Barsukova-stuchart et al. 2010]. The POP polyanion contains the largest number of palladium ions yet found in Polyoxopalladates chemistry. The bonding of each Cu^{II} ion involves the very rare eight-fold oxo-coordination, which is of significance for the antiferromagnetic interaction between them as shown in Figure 3.2. The POP molecule is negatively charged with a total charge of 20 electrons [Barsukova-Stuckart et al, 2011].

Single-crystal X-ray analysis showed that hydrated sodium salt Na₂₀[Cu₂Pd^{II}₂₂P₁₂O₆₀(OH)₈].58H₂O consists of two [CuPd₁₁P₆O₃₂] moieties connected by four hydroxo bridges as shown in Figure 3.2. POPs are double-cuboids-shaped with dimensions of 2nm × 1nm × 1nm (width x height x depth).

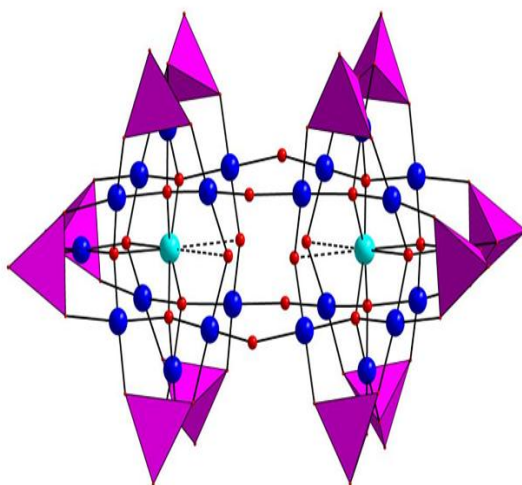


Figure 3.2 Ball-and-stick/polyhedral representation of Na₂₀[Cu₂Pd^{II}₂₂P₁₂O₆₀(OH)₈].58H₂O. Color code: Cu (turquoise), Pd (blue), O red balls, {PO₄} tetrahedral(purple). The very long Cu-O bonds [2.759(6) – 2.839(6) Å] are indicated by dotted lines; from [Barsukova-Stuckart et al, 2011].

3.2 Substrate Preparation

This section presents an overview of the substrates used in the course of this work, i.e. Au (111), and the Highly Oriented Pyrolytic Graphite (HOPG). Different cleaning techniques depending on the surfaces were applied, namely sputtering, annealing, and cleaving. Furthermore, testing the surfaces cleanliness using LEED, AES, and STM will be presented for both substrate types.

3.2.1 Gold (111)

Au has a face-centered cubic (FCC) bulk crystal structure with lattice constant of 4.08 Å [Kittel, 2005]. Au (111) is the only FCC close packed surface that shows a reconstruction [Haiss et al. 1991], namely the so-called "herringbone" reconstruction. Surface reconstruction occurs if the atoms are driven into new locations in order to minimize the surface free energy [Unertl, 1993]. We used the Au (111) surface as one of the substrates.

For Au(111), due to the effect of surface stress, the topmost layer of gold atoms is compressed along the $\langle 1\bar{1}0 \rangle$ direction, which results in a $(22 \times \sqrt{3})$ unit cell reconstruction for which 23 surface atoms are packed on 22 bulk lattice sites [Barth, 1990]. As a consequence of the reconstruction, the Au (111) surface consists of alternating domains of FCC and HCP stacking sequence, separated by corrugation lines caused by the atoms occupying the bridge sites between FCC and HCP stacking regions that are slightly displaced in the z direction. These lines appear as brighter stripes in the STM images [Woll et al. 1989] and are called the soliton walls. The reconstructed surface contains 4% more atoms than the bulk planes [Sandy et al. 1991].

The surface was prepared in UHV by repeated sputtering with Ar⁺ ions bombardment at 0.8 keV for 30 minutes followed by annealing at 900 K for 30 minutes in order to heal the damages induced by the sputtering, The Ar pressure during the sputtering process was 5×10^{-6} mbar. If the sample is stored in UHV, only heating is required to refresh the surface for subsequent experiments.

Using surface science techniques LEED (section 2.2) and AES (section 2.3), the surface structure and chemical composition can be examined in UHV just after the preparation, and before the sample is

transferred to the STM. Figure 3.3 shows Auger spectra of the Au(111) sample after sputtering, whereas the Au(111) LEED pattern is presented in Figure 3.4.

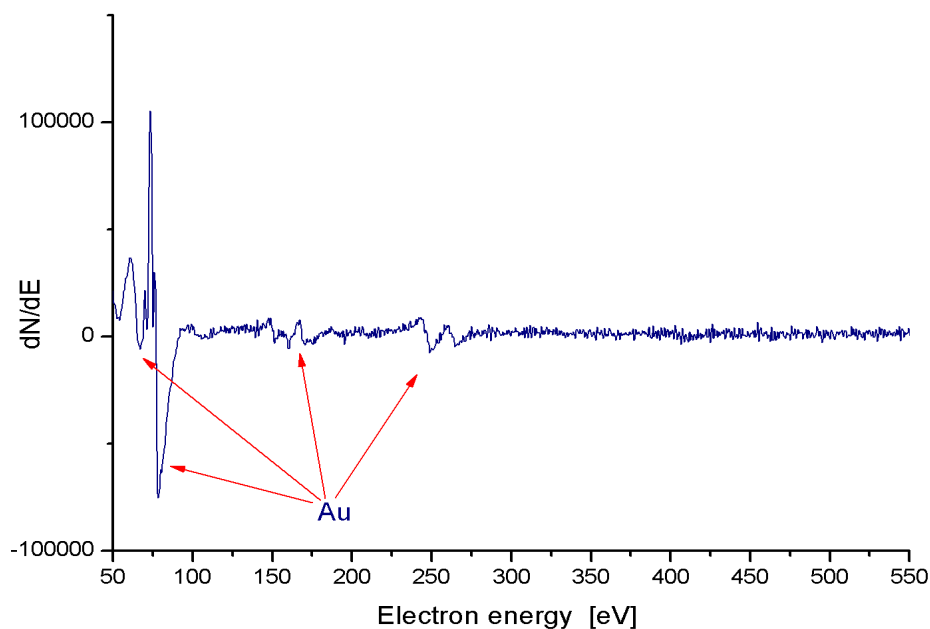


Figure 3.3 Auger spectrum of the Au (111) surface after the cleaning process indicating a clean surface. No other chemical elements can be detected. In particular, no carbon (275 eV) and oxygen (510 eV) can be observed indicating a clean surface.

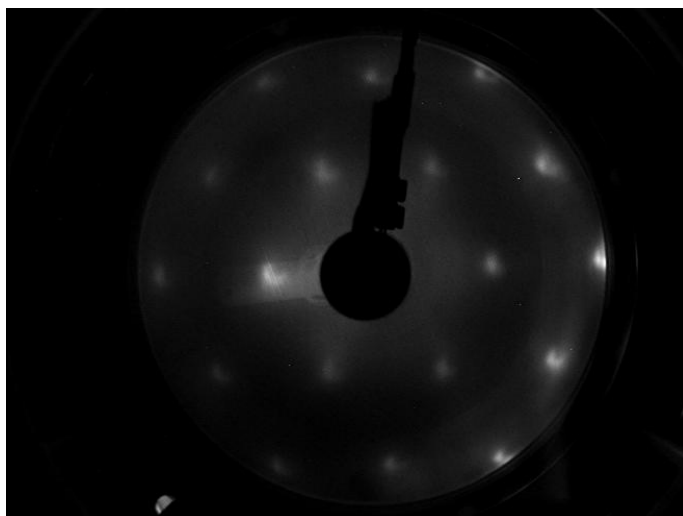


Figure 3.4 LEED pattern of the Au(111) surface (electron energy = 119.9 eV).

Figure 3.5 shows an atomically resolved STM image (panels a and b) of the prepared Au(111) crystal showing the herringbone reconstruction (panel c). The lines of the herringbone pattern

change their direction by 120° at the so-called elbow sites [Woll et al. 1989], where contaminations are preferentially adsorbed due to the locally enhanced surface reactivity.

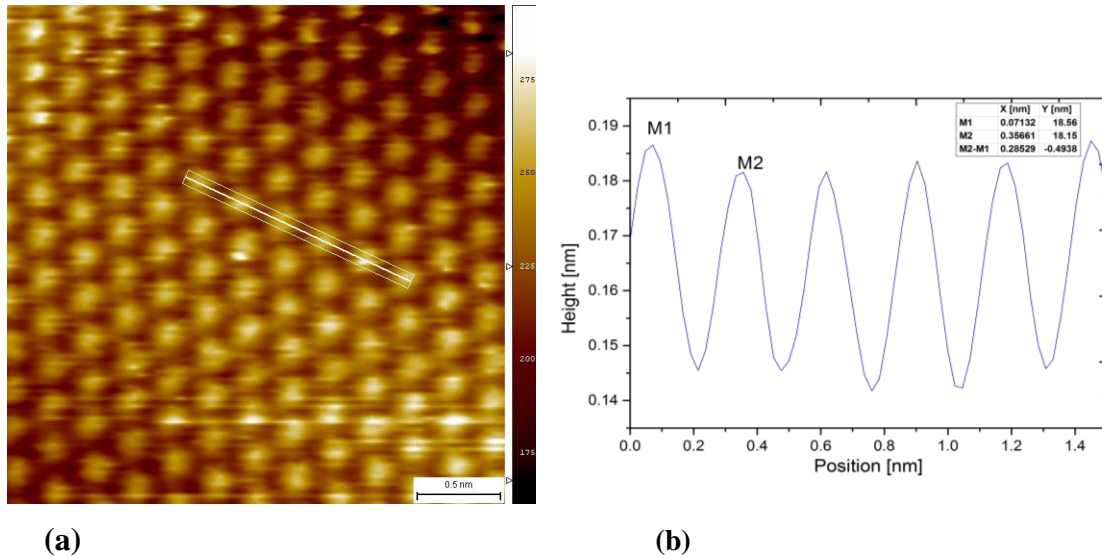


Figure 3.5 a) Atomic resolution of the Au(111) surface. Area $3 \text{ nm} \times 3 \text{ nm}$, $I_T = 0.8 \text{ nA}$, $U_{\text{gap}} = 0.5 \text{ V}$ at 77 K. b) line section along the white line in a). c) STM image of the herringbone reconstruction of Au(111). $I_T = 0.5 \text{ nA}$, $U_{\text{gap}} = 0.32 \text{ V}$ at 77 K.

The measured lattice constant of Au(111) is obtained from the lateral distance between atoms along the x-axis in Figure 3.5(b). The measured value is approximately 0.285 nm, which is comparable to the literature value within 2 %.

3.2.2 Highly oriented pyrolytic graphite (HOPG)

HOPG is obtained by heating hydrocarbons close to their decomposition temperature around 3300 K [McNaught and Willinson, 1997]. It is characterized by a higher degree of ordering compared to ordinary graphite, with an angular spread between the graphene sheets of less than 1° . The graphene layers are perfectly planar in HOPG, while in ordinary graphite they can form microscopically randomly oriented domains, making HOPG a better in-plane electric conductor than ordinary graphite. The crystal structure of HOPG is sketched in Figure 3.6.

The graphite structure consists of planar graphene layers. These layers are weakly bound to each other via van-der-Waals forces. The carbon atoms in the graphene layers are sp^2 hybridized. Therefore these orbitals take a triangular planar shape. As a consequence each carbon atom has three neighbors and forms three σ bonds with other carbon atoms in the same layer resulting in the hexagonal lattice [Shriver et al. 1994]. The fourth π orbital overlaps with the p orbitals of the graphene layers above and below. The delocalized electrons in the π bonds are responsible for the in-plane conductivity of graphite.

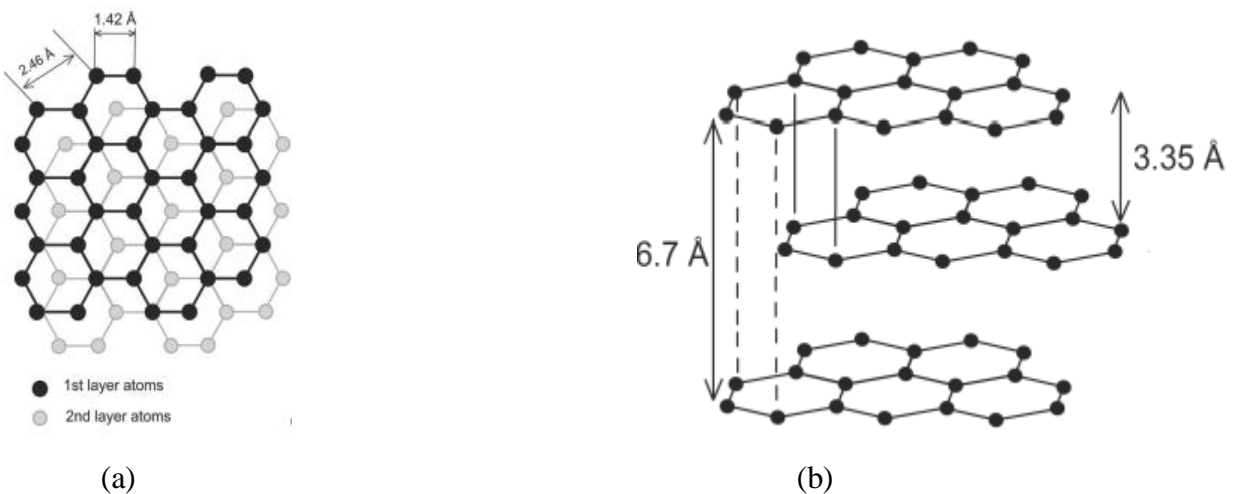


Figure 3.6 Top (a) and side (b) views of the HOPG structure [Shriver et al. 1994].

Half of the carbon atoms in each plane are situated directly on top of the atoms of the layer underneath, while the other half is located at the centers of the hexagons of the layer below. This explains the emergence of “small and large” hexagons in STM images [Batra, 1987].

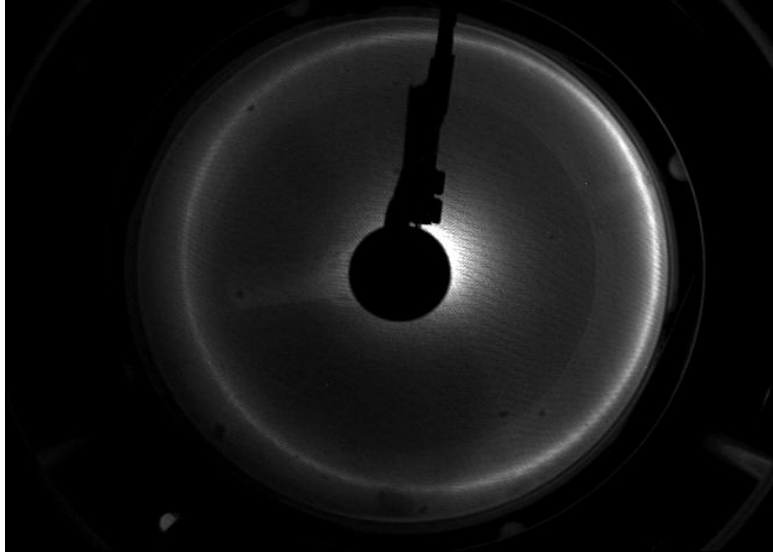


Figure 3.7 LEED pattern of the HOPG surface (with electron energy 92.3 eV).

The HOPG surface was prepared by cleaving of the topmost layers using adhesive tape immediately prior to introducing the sample into the UHV. Figures 3.7 and 3.8 show the LEED pattern and AES data for the HOPG sample followed by an STM image with atomic resolution of the HOPG surface as shown Figure 3.9.

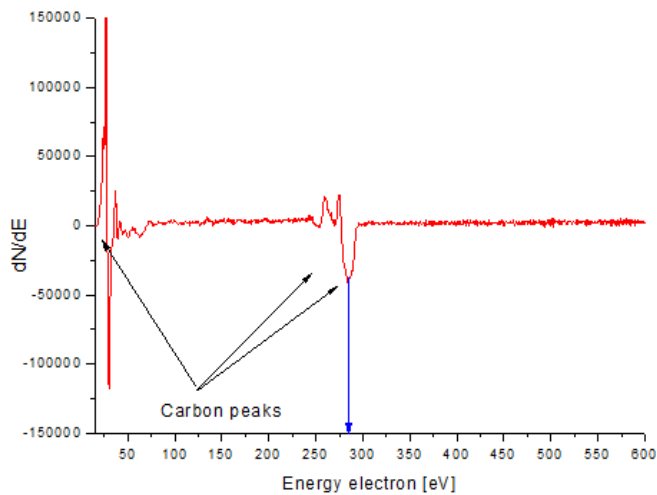


Figure 3.8 Auger spectrum of the HOPG surface after the cleaning process. The blue arrow indicates the main peak of carbon (275 eV).

Figure 3.7 shows a LEED pattern from the clean HOPG surface. It consists of rings instead of spots because HOPG comprises a large number of micron-size crystallites having random in-

plane orientations, and the diffraction pattern is an incoherent superposition of many single-crystal diffraction patterns [Ferralis et al. 2004].

The selected black hexagon in Figure 3.9(a) presents the small hexagon of carbon atoms. The measured lattice constant is obtained from the lateral distance between atoms in x-axis as shown in Figure 3.9 (b). The measured value here is approximately 0.23 nm, which deviates from literature value by 6 %.

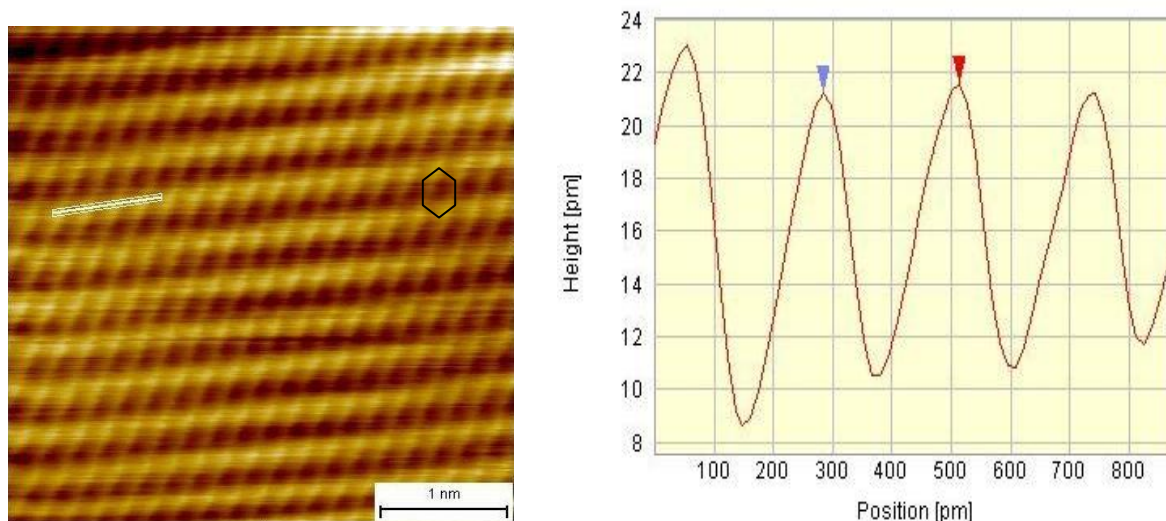


Figure 3.9 (a) Atomically resolved STM imaging of the HOPG surface. $4 \text{ nm} \times 4 \text{ nm}$, $I_T = 0.2 \text{ nA}$, $U_{\text{gap}} = 0.5 \text{ V}$ at 77 K . (b) Line section along the white line in (a).

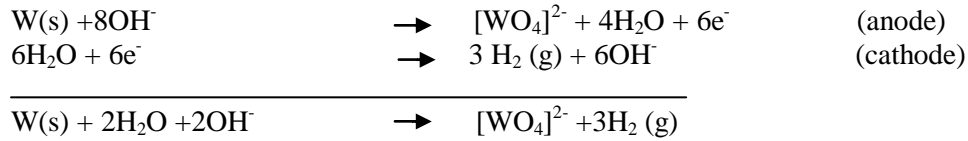
3.3 Drop Casting Method

The simplest way to assemble molecules on a substrate is through direct deposition. That was carried out by the drop casting method, where a droplet of solution is applied onto the substrate by a pipette (Figure 3.10), and then the solvent is slowly evaporated. Four different concentrations of POPs (10^{-8} , 10^{-7} , 10^{-6} and 10^{-5} molar) were examined. A droplet of $50 \mu\text{L}$ of POPs solution of each concentration was drop-casted onto Au (111) and HOPG surfaces, and the H_2O solvent was left to evaporate for 1 hour under ambient conditions.

3.4 Tungsten Tip Preparation

The stability and sharpness of the tip plays a curial role for STM measurements to obtain high quality surface structure topography. In this work, the electrochemical etching method was applied to produce sharp W-tips.

A piece of a polycrystalline tungsten bulk wire with a diameter of 0.38 mm was mounted to a holder. Two pieces of plastic tube were applied with a small gap of about 1 mm to limit the etching area. The prepared wire was immersed into caustic soda solution (NaOH) as shown 8in Figure 3.11. A ring-shaped platinum wire was situated around the W wire and served as a cathode. When a DC voltage is applied between the tungsten wire and platinum ring, the following reactions take place:



Solid tungsten is oxidized to tungstated $[\text{WO}_4]^{2-}$, while at the cathode hydroxide ions (OH^-) and gaseous hydrogen are produced. The etching process of the lower part was terminated when the entirely etched wire dropped off. We used the lower part as STM tip. A plastic disk at the bottom end of the tungsten wire protects the lower part from hitting the glass container when it falls down. The resulting tip apex has a curvature radius of typically 20 nm. After rinsing the tip in distilled water to get rid of the remains it was dried with clean nitrogen gas. The tips then were ready for transfer into the UHV system.

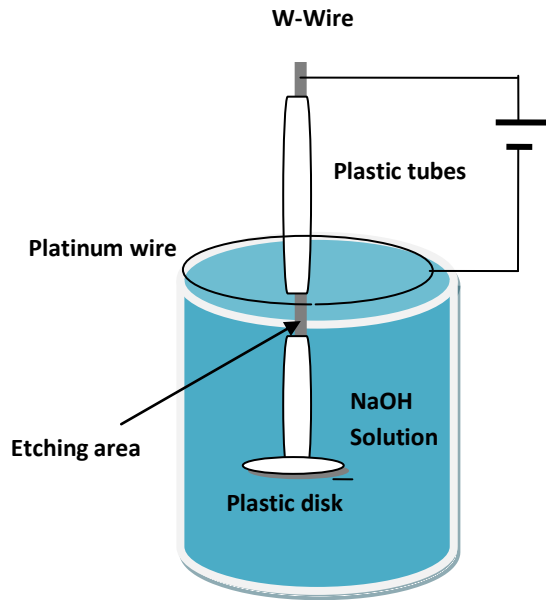


Figure 3.10 Setup of the electrochemical etching of the W-tips. The etching takes place at the small region around the W-wire that is immersed in the caustic soda solution (NaOH) and is not protected by the plastic tubes.

Chapter 4

Results and Discussion

In this chapter the experimental results are presented and interpreted. At the beginning we describe the experimental conditions and demonstrate by AES the successful adsorption of POP molecules on the chosen substrates. For the rest of the chapter we present the STM images of POP molecules on the Au and HOPG surfaces.

On the Au (111) surfaces with low POP concentrations we repeatedly observed chain-like structures with a width, which was large and inconsistent with the molecular size. These wide lines are appreciably different from the HOPG case, in which sharply defined chains and arrays of POP molecules were formed. On HOPG, intact molecules with different orientations and various arrangements in ordered arrays were imaged with high topographic resolution in many cases.

4.1 Experimental Conditions

The experiments were performed in an ultra-high vacuum system with a base pressure below 5×10^{-11} mbar. Before deposition, LEED and low-temperature STM surface analysis confirmed clean substrates. Depositions were carried out *ex-situ* by drop casting.

It was crucial to choose adequate substrates that are not affected by air exposure. Au(111) and HOPG satisfy this requirement. Approximately 50 μ L of POP solutions was deposited onto the clean Au(111) or HOPG substrates and dried for 1 hour in each case. All STM images presented in this chapter were taken at 77 K using W-tips, which were electrochemically etched *ex-situ* without further *in-situ* treatment. All STM images were taken in the constant-current mode of STM operation.

4.2 AES of POPs adsorbed on Au (111) and HOPG substrates

Firstly we checked the adsorption of POP molecules on the substrates. AES analysis was used to check the chemical composition of the surface before and after deposition.

The data indicates that POP molecules did indeed adsorb on the surfaces, as new peaks appeared in the spectra corresponding to the chemical composition of the POP molecules such as Pd and O. The relative peak intensities depend on the amount of the respective elements in the molecular composition.

The peaks were relatively weak for low concentrations. Therefore, the experiments were repeated with higher concentrations (i.e. 10^{-6} molar). Figures 4.1(a,b) give evidence for the adsorption of POP molecules on both Au(111) and the HOPG substrates.

Although AES data proved the presence of POP molecules on the substrates, no observation of POP molecules in STM images could be obtained for high concentrations in spite of several attempts for each substrate. A possible cause could be the disordered arrangements of the molecules for the high coverage resulting in a relatively “thick” molecular film. This possibility was confirmed after we were able to take clear images when we used the lower POP concentration (10^{-8} molar) as demonstrated in following sections.

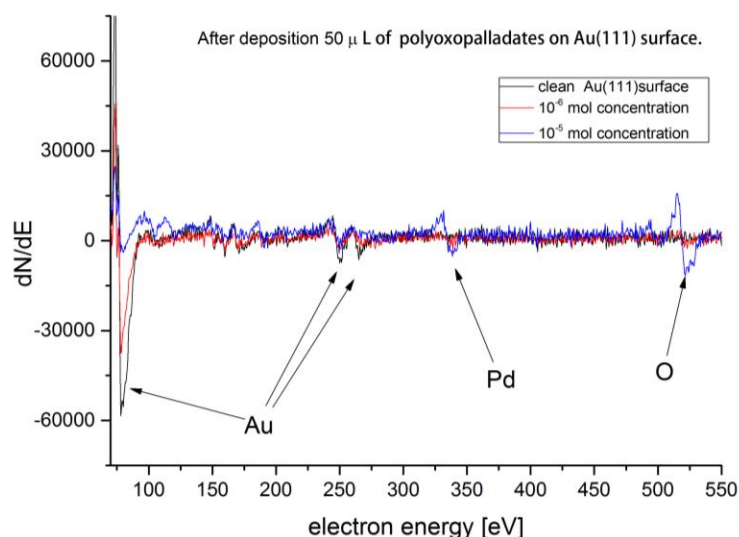


Figure 4.1 (a) Auger spectrum after deposition POPs from different solutions onto Au (111) substrates.

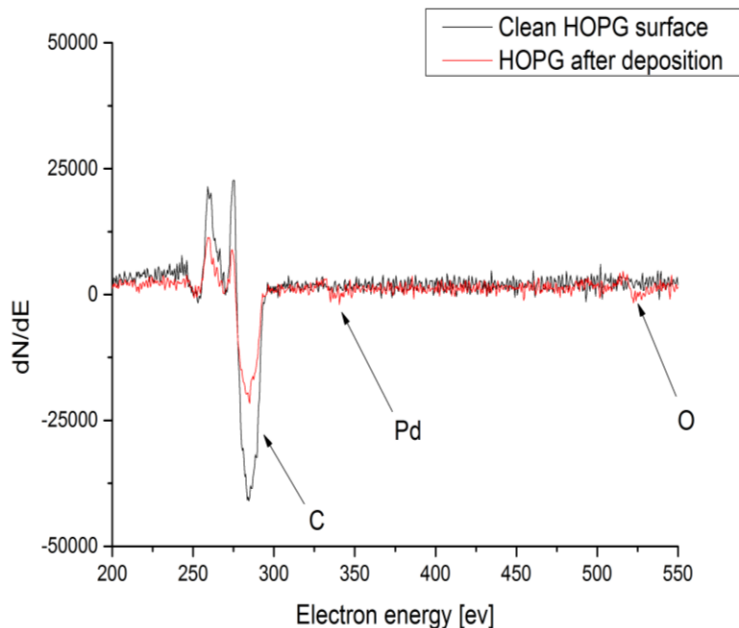


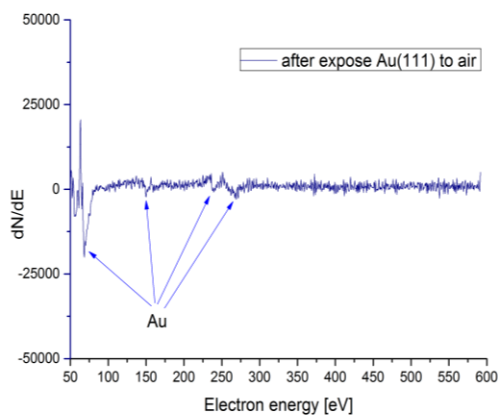
Figure 4.1 (b) Auger spectra before and after deposition of 10^{-7} molar of POP solution onto HOPG surfaces.

4.3 POP molecules on Au (111) surface

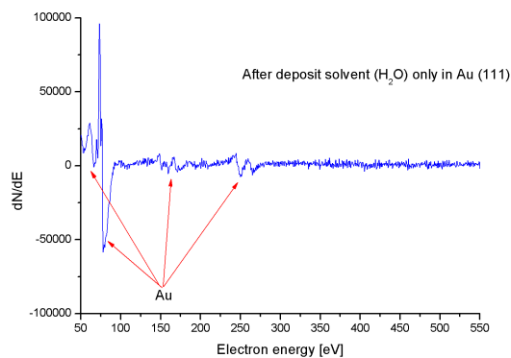
After the preparation of the Au (111) surface we insured that the surface is clean by STM investigations. No contaminations on the terraces were observed in the STM images, and atomic resolution and images of the herringbone reconstruction were obtained, as shown in Figure 3.5.

The sample was then transferred to the load-lock chamber via the transfer rods. Since the deposition was done *ex-situ*, the load-lock chamber was vented and opened. Before depositing the POPs two points were considered. The first is the effect of air exposure on the sample, and the second is the effect of the pure solvent (H_2O). AES analyses showed that no other chemical elements were detected on the surface after the air exposure [Figure 4.2(a)] and exposure to the solvent only [Figure 4.2(b)]. In particular, no carbon (275 eV) and oxygen (510 eV) peaks could be observed.

The resistance of the Au (111) surface against air and solvent exposure was also confirmed by the STM measurements shown in Figure 4.3, which are taken after reinserting the sample into the UHV system.



(a)



(b)

Figure 4.2 Auger spectra of the Au(111) substrate after expose to air (a) and to the solvent only (b).

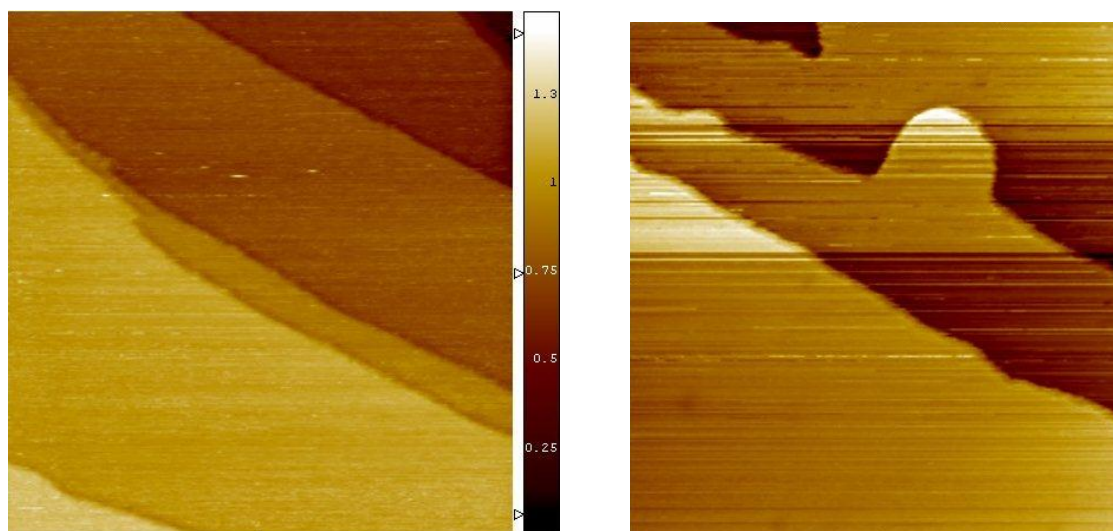


Figure 4.3 (a) STM image after exposure of the Au(111) surface to air showing terraces. The 200×200 nm image is taken at $I_T=1$ nA, $U_{\text{gap}}=0.5$ V. (b) STM image of the Au(111) surface after depositing the solvent (H_2O) only. The 50×50 nm image is taken at $I_T=1$ nA, $U_{\text{gap}}=1$ V at RT^\dagger .

Spatially resolved topographic images of POPs on the Au (111) substrate were feasible only for the lowest POPs concentration (10^{-8} molar). Still the images showed wide, and poorly ordered lines or chains on the Au (111) substrate.

The POP molecule is about 2 nm wide, whereas the lines were approximately 10 times wider. The lines could be an aggregation of POP molecules, formed due to intermolecular and

molecule-surface interactions. The line structure is shown in Figure 4.4. The z-profile shows that the line height is about 20 pm, and that is consistent with the height of POPs deposited on the HOPG substrate.

Zooming into Figure 4.4(a) reveals an internal line structure as shown in Figures 4.4(c) and (d). That however, does not give clear evidence that the lines are formed by POP molecules, and more STM observations at higher resolution are required to definitely understand the line structures.

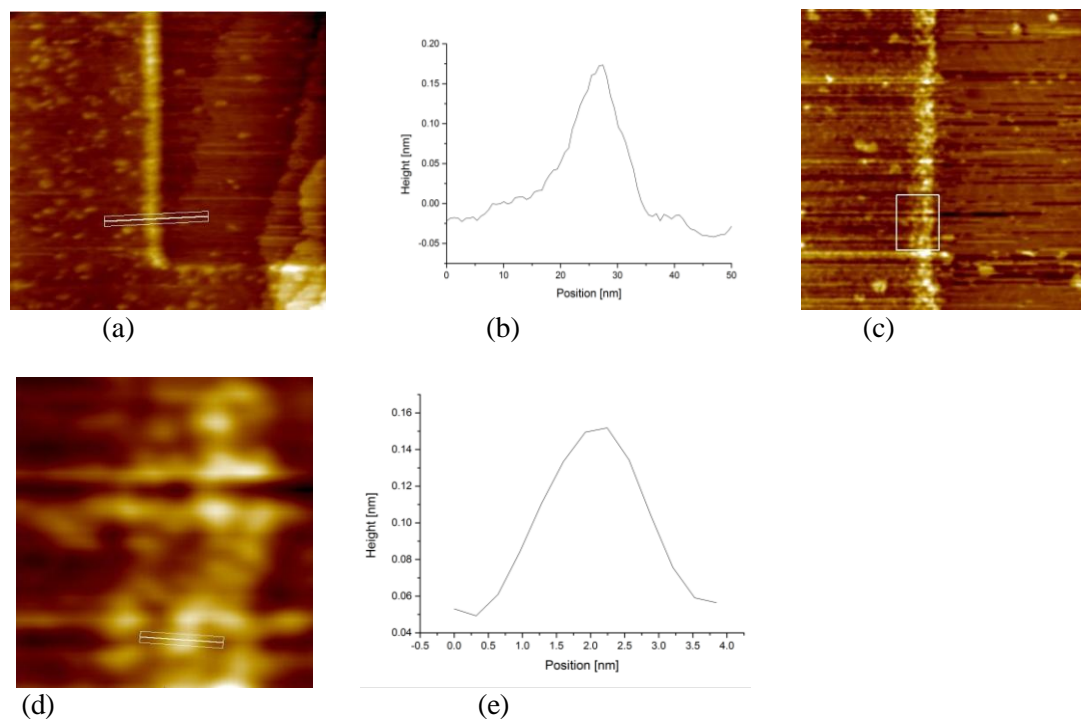


Figure 4.4 (a) STM image of a line structure on Au (111) after adsorbing POP molecules from an aqueous solution. Terraces and some contamination are visible on the right side; Area = $200 \times 200 \text{ nm}^2$, $I_T = 0.15 \text{ nA}$, $U_{\text{gap}} = -0.55 \text{ V}$. (b) Line section along the line in (a). (c) Zooming into the line in (a) showing the herringbone structure of the Au (111) substrate. (d) Zooming into the selected rectangle in (c) shows the contrasts inside the line structure. (e) Line section along the white line in (d).

The large width of the lines suggests formations of condensed aggregations of POPs. A possible reason for the formation of elongated, chain-like structures may be a molecular alignment along the step edge between two terraces, where the surface edge can create stronger attraction for the molecules. Another less possible reason is that the chains actually follow the herringbone reconstruction structure by filling the region between two along the soliton walls as discussed in

section 3.2. The absence of large scale ordering of the chains according to the unperturbed herringbone reconstruction [Figure 3.5(c)] could be explained by a partial lifting of the reconstruction during the deposition process. All of these proposed explanations however are not based on clear evidence and can be treated as speculations.

4.4 POP molecules on the HOPG substrate

HOPG is one of the best-studied substrates both experimentally and theoretically due to its specific electronic properties [Matsui et al. 2005]. The 10^{-8} molar POP solution was drop-casted on the HOPG substrate and dried under ambient conditions for 1 hour. STM images of HOPG samples prepared with this concentration revealed the best results.

4.4.1 Well-ordered POP lines on the HOPG surface

The molecular arrangement of POPs on the HOPG surface reported here is produced for the first time. Figure 4.6 shows one of the images that reveal a well-ordered POP molecular chain aligned along the graphite surface. Individual molecules are easily distinguished and the spacing is a result of the strong repulsive interaction between the negatively charged POP molecules as mentioned in section 3.1. The size of a single molecule in Figure 4.6 is approximately 2 nm, which is comparable to the actual molecule size.

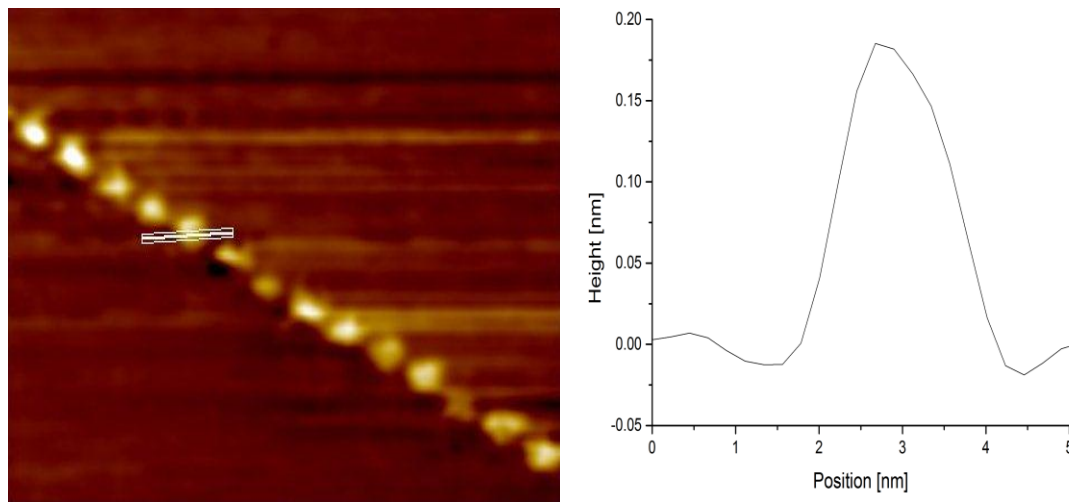


Figure 4.5 (a) STM image of double-cuboid-shaped POP molecules on the HOPG surface, area $32.2 \text{ nm} \times 22.1 \text{ nm}$, $I_T = 1.5 \text{ nA}$ and $U_{\text{gap}} = 3 \text{ V}$. (b) The molecule height and width are indicated by the line section along the white line.

To understand how the molecules are arranged on the substrate, we moved the STM image frame along one molecular chain and got the following observations: The chain starts from a step edge and ends also at a step edge.

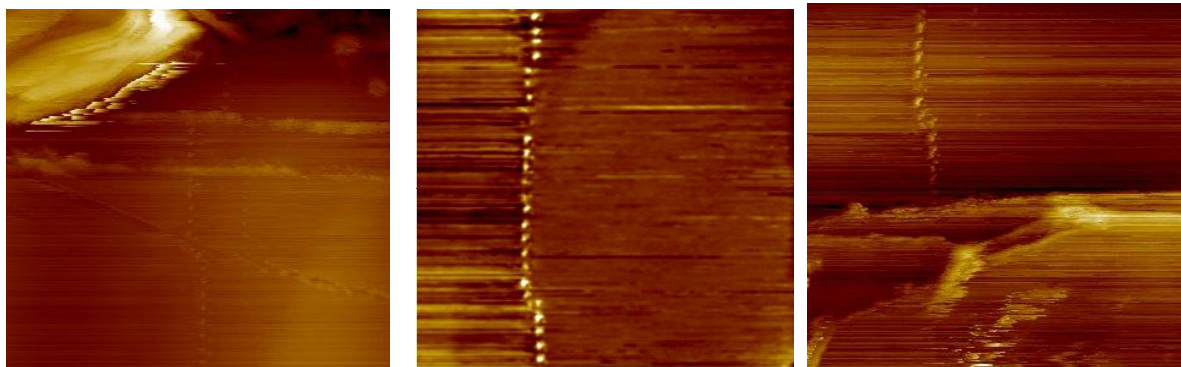


Figure 4.6 STM images of selected sections of a 430 nm long molecule chain. (a) Upper end of the chain, (b) middle part, and (c) lower part of the chain also showing HOPG steps. The 125 nm \times 125 nm images are taken at $I_T = 1.5$ nA and $U_{\text{gap}} = -0.5$ V.

The areas beyond these big edges were scanned and showed no POP molecules. The chain length was approximately 430 nm and it was not completely straight. A second chain appears from the side and runs parallel to the main one and then bends away to the side see Figure 4.7.

We studied other molecular chains in order to determine their capability of crossing HOPG steps or getting trapped along the steps of the HOPG substrate. We selected a chain that was located near two close HOPG steps. The STM image of Figure 4.8 for a selected part of the chain shows that it indeed crosses the HOPG steps. Consequently, monatomic graphite steps do not determine the chain formation.

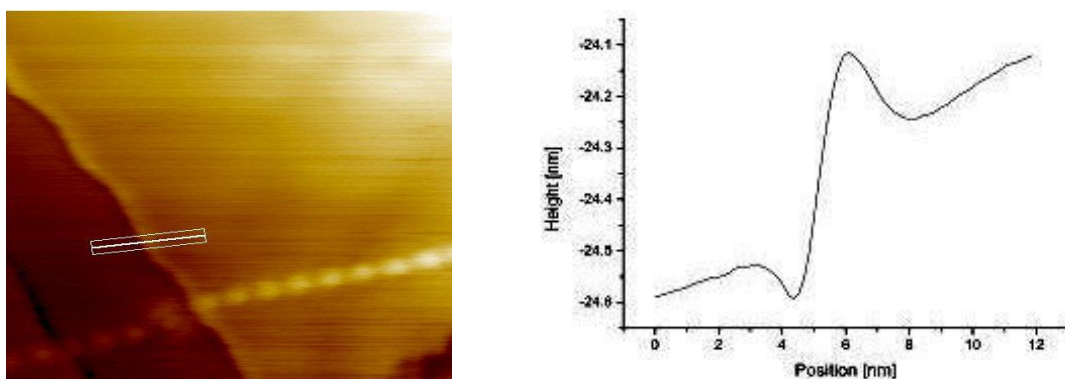
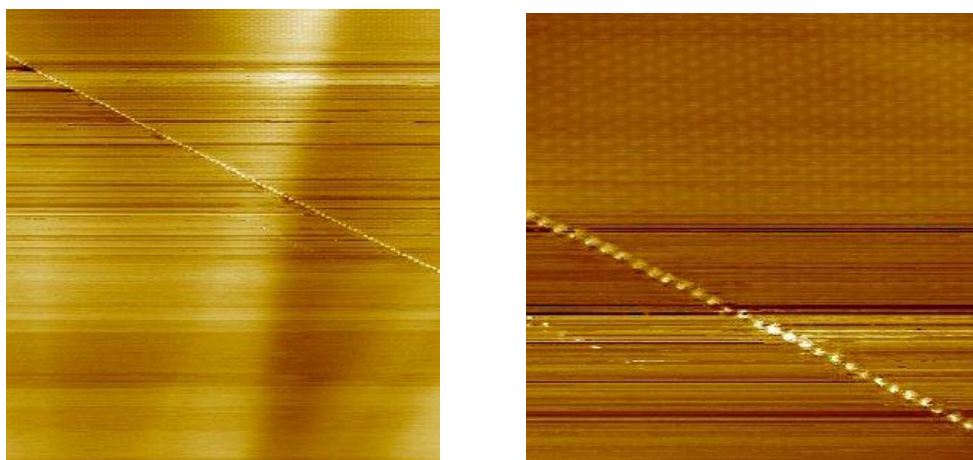


Figure 4.7 STM image taken with $I_T = 1.5$ nA, $U_{\text{gap}} = -0.1$ V, and scan area 46.3×46.3 nm² showing a molecular chain crossing HOPG steps (a) and a cross section of the substrate step revealing its monatomic height (b)

4.4.2 Observation of molecular chains and arrays on HOPG

Figure 4.9 shows large scan-area images of highly regular patterns that we attribute to well-ordered arrays of POP molecules arranged on the graphite surface. The pattern is only visible at the right upper side of the molecular chain [best visible in Figure 4.9(b)] that runs through the image.



(a) (b)
Figure 4.8 (a) STM images of large scan-area of POPs showing both a molecule chain and a molecular array on HOPG. (b) A selected part from (a) showing better resolution especially for the molecule array. Scan area (a) = 180 nm × 180 nm, (b) = 66.6 nm × 66.6 nm, $I_T = 1.5$ nA and $U_{\text{gap}} = 3$ V.

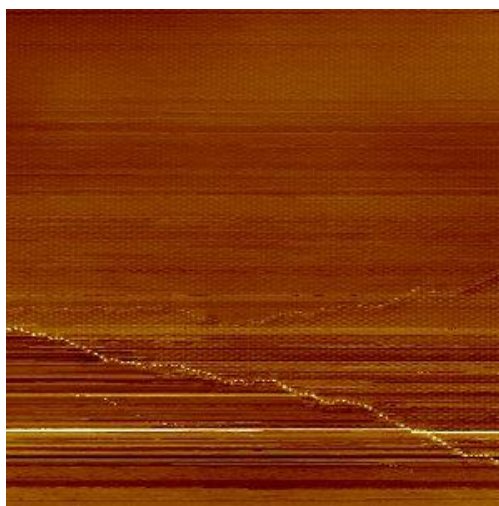


Figure 4.9 Large scan area STM image for POPs on a HOPG surface. The POP array extends from the molecule chain at the bottom up to the top of the image. Scan area 200 nm × 200 nm, $I_T = 1.5$ nA and $U_{\text{gap}} = 3$ V.

Although the molecular array is not obvious in the whole area in the right upper side of the molecule chain, images can be produced after repeated scanning with relatively mild tunneling conditions (i.e. 1-1.5 nA). In contrast, the left lower side of the molecule chain does not show evidence of a molecular array under any tunneling condition. Therefore, it seems that the chain is the edge of the array. Other totally different areas were scanned and they yielded similar results. An example is given in Figure 4.10.

These arrays exhibit periodicities consistent with the molecule size of 2 nm. Thus, the imaged arrays suggest that we are observing monolayers of POPs on graphite. Figure 4.10 shows a monolayer array of POP molecules covering the area from the first molecular chain boundary up to the top of the STM image. The recorded chain is located at the array edge.

Figure 4.11 shows a high-resolution image of a molecular array. The protrusions are arranged in a hexagonal closed pattern. Our data represent the first evidence of POP formations of arrays on HOPG.

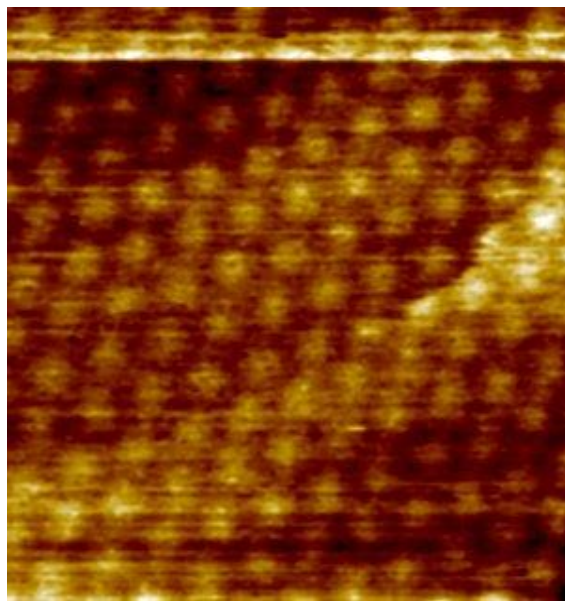


Figure 4.10 STM images of molecule arrays on HOPG. The scan area is $20 \text{ nm} \times 20 \text{ nm}$, $I_T = 1.5 \text{ nA}$ and $U_{\text{gap}} = 1 \text{ V}$.

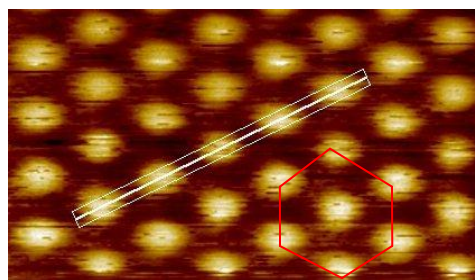
From further STM measurements of the same sample we were able to observe two types of molecular arrangements. The first are mainly straight molecular chains with different

orientations as discussed in section 4.4.1. The second are molecular arrays as discussed in this section. Many images showed the chains located at the edges of ordered molecular arrays. It cannot be confirmed however, if this is always the case because the corrugation of the arrays is very small and its appearance in the images strongly depends on the resolving power of the STM-tip.

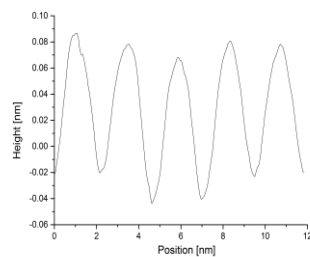
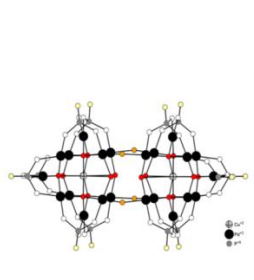
At present it is not clear if the bright chains at the edges of the arrays appear in the STM images due to a true structural “fence” of the arrays (e.g. different, e.g. upright molecule orientation or double-layer stacking) or due to an electronic effect that leads to a much higher tunneling current (and thus an apparent elevation) at the edge. Both possibilities could originate from the missing of molecular neighbors on the outer side of the array and the related reduced local symmetry, similar to the formation of reconstructions and electronic surface states at surfaces. In this sense, the array edge is the 1-dimensional analogue of 2-dimensional surfaces. A possible explanation for the formation of array edges at certain locations could be grain boundaries of the HOPG substrate or dents created during the cleaning of the surface.

4.4.3 Molecular Arrays Comparison

Although, obtaining STM images of molecular arrays is difficult, we were able to map them several times. Most often the sub molecular resolution image of each single molecule in those molecular arrays appears as spherical structure with a size of approximately 2 nm. The z-profile shows that the apparent height of the molecule in the arrays is about 100 pm as was the case for the z-profile images recorded within molecule arrays.



a)



b)

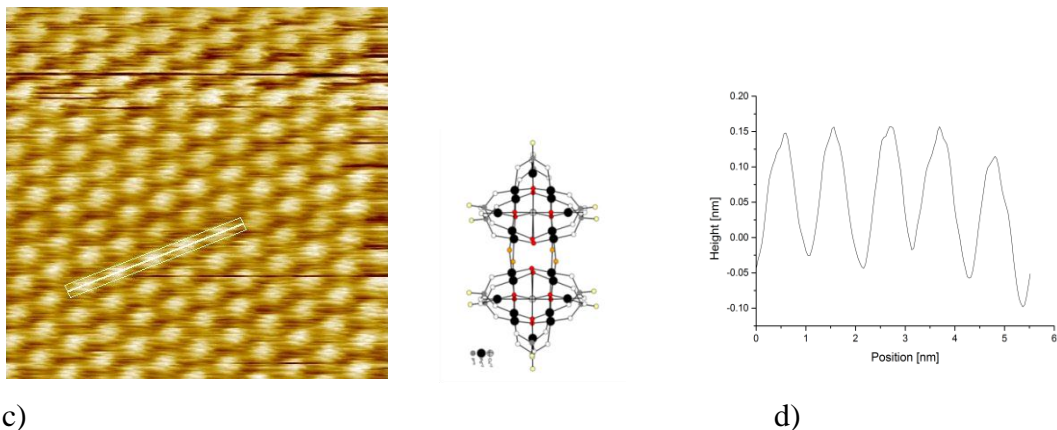
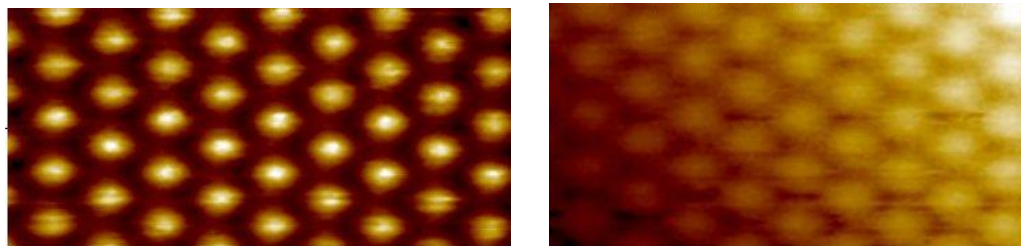


Figure 4.11 (a) High-resolution STM topography of a densely packed of POP molecule arrays on HOPG surface with the unit cell of the superstructure as indicated by red lines with hexagon shape with one molecule on the center (size area = $17.3 \text{ nm} \times 9.8 \text{ nm}$, $I_T = 1.5 \text{ nA}$ and $U_{\text{gap}} = 3 \text{ V}$). (b) a cross section along the white line in (a). (c) STM image of molecule arrays with different geometry size and height (size area = $11.1 \text{ nm} \times 11.1 \text{ nm}$, $I_T = 1.5 \text{ nA}$ and $U_{\text{gap}} = 3 \text{ V}$). (d) Cross section along the white line in (c).

However few STM images recorded molecular arrays with half the lattice constant (1 nm), but doubled z-profile height (200 pm). This suggests that either the molecules in these cases are standing upright on the HOPG surface or broken into single-cuboid molecules. Figure 4.12 shows high-resolution STM images of molecular arrays for both cases. The unit cells of the molecular arrangements are determined and marked. Both arrays are simple hexagonal Bravais lattices and reflect the symmetry graphite lattice.

4.4.4 Molecular array structure as a function of the tunneling current

STM images are dependent on the charge distribution on the molecules. When the charge density is large, we expect an increase in the tunneling current, yielding brighter STM contrast and visa versa: darker STM contrast for low charge density. In the constant-current mode the distance is varied to keep the current constant. The tip is retracted (approached) in areas with high (low) current density, and the recorded z-piezo signal yields accordingly bright (dark) contrast.



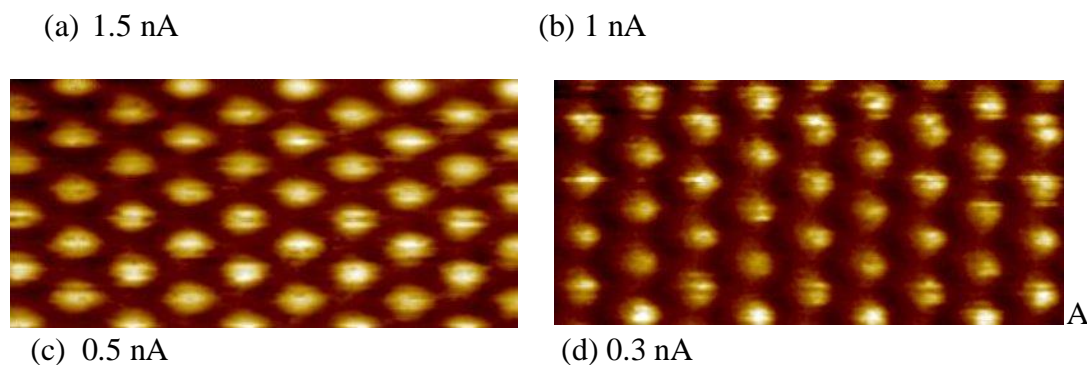


Figure. 4.12 Constant-current STM images of molecular arrays of POPs on the HOPG surfaces for different set tunneling current values. Tunneling current in (a) 1.5 nA, (b) 1 nA, (c) 0.5 nA and (d) 0.3 nA. [(a) – (d) area = 20 nm × 10 nm and $U_{\text{gap}} = -0.5$ V]

We took images under the constant-current mode for a number of set-point current values to obtain information about the intermolecular structure. When we increase the set-point current we operate closer to the surface and vice versa. This means the scan maps iso-surfaces of different charge densities values resulting in a variation of the molecular profiles. By changing the set-point current we want to obtain information about the intra-molecular structure of the POPs.

Figure 4.13 shows small changes of the molecule shape from spherical as shown Figure 4.13(a) to elliptical in Figure 4.13(c). The elliptical shape in Figure 4.13(c) could be an indication that the cuboids are laying flat on the HOPG surface in the case of dense arrays. A detailed analysis of the image variations in Figure 4.13 can only be done in combination with theoretical calculations of STM images that properly describe the decay of the wave functions above the surface or molecules into the vacuum region. States with clearly different decay lengths into the vacuum are predominately imaged for very low or high set-point current, respectively.

4.4.5 Molecular array profile dependence on the bias voltage

High and low charge densities can be addressed by varying the bias voltage to see if the density of states (DOS) shows significant energy dependence, e.g. a gap close to the Fermi level with HOMO/LUMO states at certain energies.

Figure 4.14 displays constant-current images taken at selected bias voltages applied to POP molecules on the HOPG surface. In each image the molecules appear as bright elliptical shapes.

At some bias voltage and in some regions atomic resolution of HOPG appears in addition to the molecular contrast as shown in Figure 4.14(c-d).

It would be interesting to investigate the electronic structure of the molecules by Scanning Tunneling Spectroscopy (STS) to obtain clear evidence for the adsorption geometry of the molecules and a clear identification if they are single-cuboid or double-cuboid POPs.

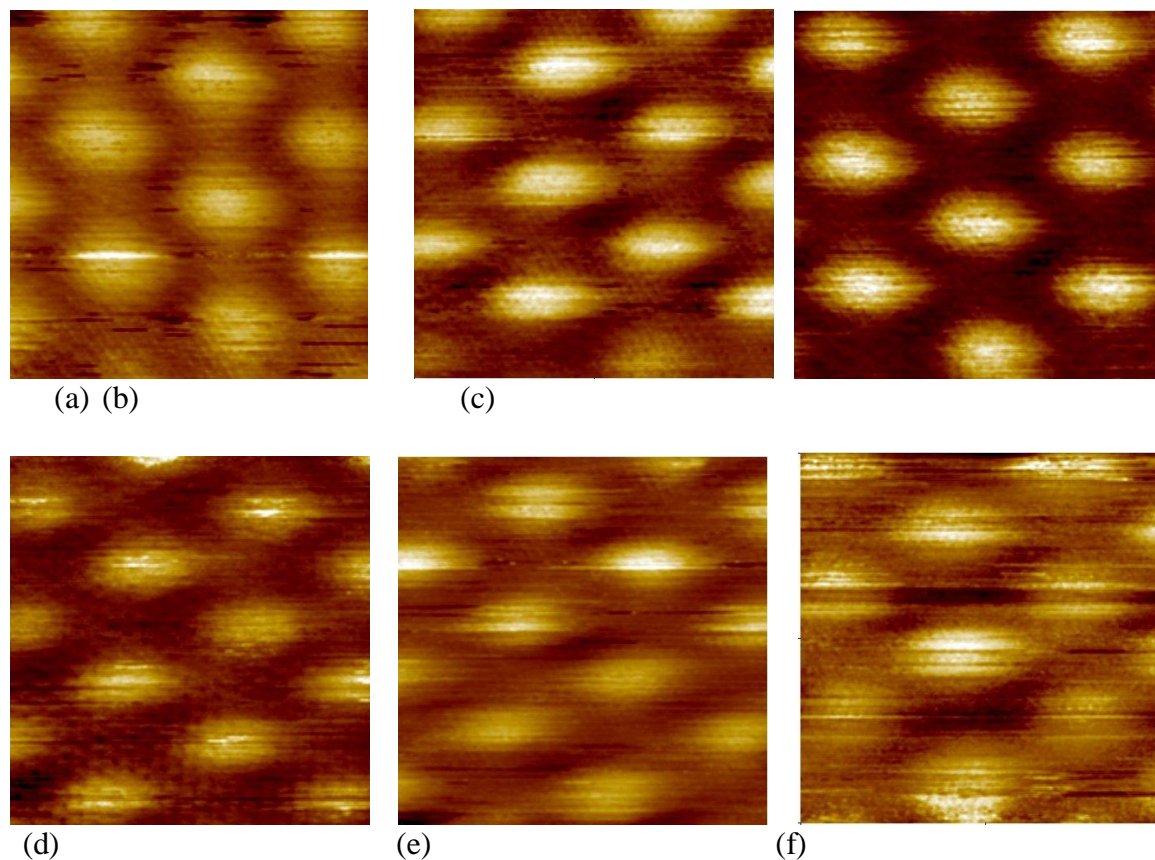


Fig 4.13 Constant-current STM images of POP molecules on the HOPG surface as a function of the bias voltage. Bias voltage (a) 1.5 V, (b) 2 V, (c) 3 V, (d) -0.1 V, (e) -0.3 V, (f) -2 V. [(a) – (f) image area 6.67 nm \times 6.67 nm and $I_T=1.5$ nA]

4.4.6 Double layers of the molecular arrays

Figure 4.15 shows a POP molecular array with some irregularities in the lattice. It seems that the molecules conglomerate above each other in some regions and thus appear brighter in the STM image (blue circle). To investigate this argument we produced a z-profile along one row of protrusions along the white line in Figure 4.14(a) as displayed in Figure 4.14(b). The blue circle

marks two protrusions, which are three times higher than the others located next to them, whereas the green circle marks two neighboring protrusions, whose height differs by one typical protrusions height. A conclusive interpretation of this variation is difficult because such defects could have been induced by irregularities (point defects, steps) of the HOPG substrate.

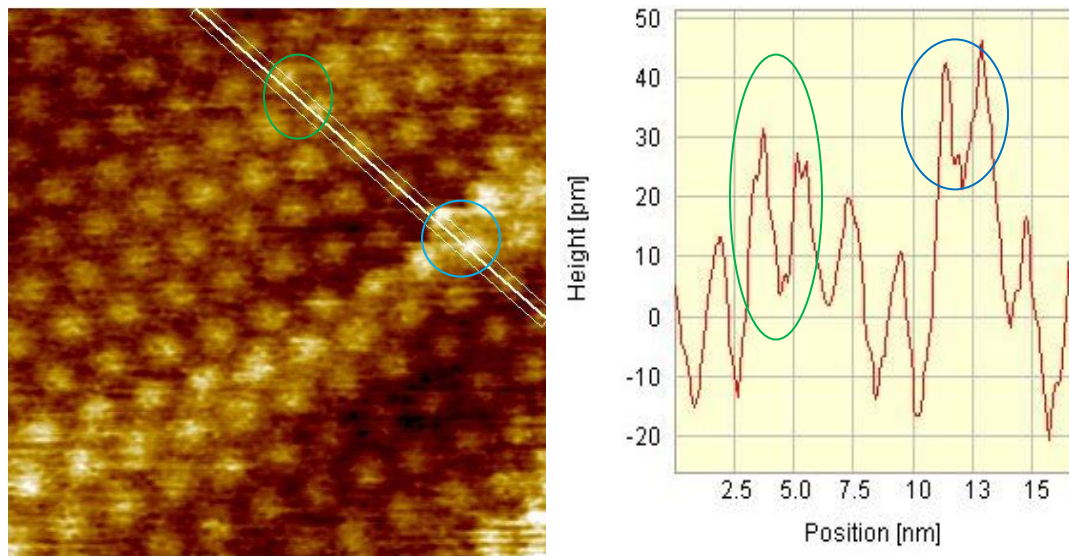


Figure 4.14 (a) Constant-current STM topography of a POP molecule array on the HOPG surface showing a non-uniform lattice with a dislocation (blue circle). (b) Line section along white line in (a). Image size $20 \text{ nm} \times 20 \text{ nm}$, $I_T = 1.5 \text{ nA}$ and $U_{\text{gap}} = 1 \text{ V}$.

Chapter 5

Summary and Conclusions

Molecules on surfaces play a fundamental role in many fields of interest like heterogeneous catalysis, epitaxial thin film growth, molecular electronics and formation of nanostructures in general. The main objective of this thesis was to investigate the adsorption characteristics of double-cuboid insulating POP molecules on two differently reactive substrates, namely Au(111) and HOPG substrate.

We used these substrates because they are unaffected by air exposure since deposition is performed *ex-situ*. Alternatively POP molecules were chosen because they are stable in the solid state under air, and they have the potential of being used as precursors in spintronics devices. In addition there are no previous STM studies reported for these molecules.

We studied first the dependence of the POP adsorption on the substrate type using AES followed by a detailed investigation of the STM topography of the molecules adsorbed on the substrates. The results were consistent for the HOPG but did not settle well for the Au surfaces. In the following we summarize our observations and conclusions:

1. POP chains on HOPG were formed and clear images were produced. The chain height and width were consistent with the molecular size for various orientations. The images were best and useful for the low concentration (10^{-8} molar).
2. We observed with high resolution the formation of arrays with chains at the edges. The chains length reached more than 400 nm, and the molecular height varied from 100 pm for the arrays to 200 pm for the molecular chains.
3. POPs are usually images with spherical profiles. Under certain bias conditions the images change to an elliptical appearance possibly indicating that the molecules were flipping from standing upright to laying along the surface or that they have broken into single-cuboid molecules. A complete understanding requires comparison to detailed electronic structure calculations.

4. No images were obtained for concentrations larger than 10^{-8} Mole/liter for both HOPG and Au (111): The film structure is expected to change as a result of multilayers formation that can smear the structure. In addition, the molecular interactions can bring higher influences on the disordering of molecules.
5. Wide adsorbate lines were observed systematically on the Au surface for the low concentrations. The width exceeded 10 times the molecular size. In contrast, the chains formed on the HOPG surface were clearly ordered and neatly preserving very sharp lines and even forming arrays. The variance between the two cases reflects different molecular-surface interactions. It seems for the HOPG surface intermolecular interaction is prevailing over the molecule-surface interaction and controls the adsorbate arrangement, whereas in the case of gold the molecule-surface interaction is more influential. Surface defects of the substrate such as the terrace structure or remainder of the herringbone reconstruction are likely to be responsible for the chain formation due to the locally enhanced interaction. The irregular arrangement of the chain supports this explanation.
6. These arguments are further supported by the fact we were unable to get any clear images when we used higher concentrations, which lead to multi-layering and thus a weakening of the influence of the substrate on the molecular ordering. The resulting disordered molecule arrangement prevents successful STM imaging.

Recommendations

We recommend conducting the following tests and measurements as a follow-up to our work. They are also summarized in the table 5.1.

1. Use LEED to get a reciprocal space characterization with of the molecular arrays. Even though our images have shown stable arrays over a reasonable area (200 nm* 200 nm) the overall surface of the substrate covered by the POPs is over 1000 times this size. It will be desirable to see the overall profile of the POPs formation over the wide surface.

2. Scanning Tunneling Spectroscopy (STS) offers the possibility to investigate the LDOS structure with lateral atomic size resolution. Using the differential conductivity of the sample dI/dV as a function of the applied bias voltage *may provide some detailed* information about the density of states. This will help understand the internal electronic structure, e.g. HOMO-LUMO gap, and provides data that can be compared to electronic structure calculations.
3. The measurements on the Au surface did not yield satisfactory understanding of the adsorption of the POP molecules and the preferred adsorbate arrangements. Redoing the measurements on Au (111) at lower concentration may help to unravel the influence of the soliton walls of the herringbone reconstruction or the terrace structure on the adsorption process.
4. POP adsorption on HOPG at much smaller concentrations could produce isolated smaller arrays. Even though this could be hard to achieve, a test of this kind may shed some light on the dynamics of the molecular profile structures. We propose using (STM, AES, and XPS) for different POP lower concentrations.
5. As discussed in section 4.4.3 we imaged POP arrays with lattice constants measuring half the molecule size and twice its height. We asked the chemistry group to synthesize single-cuboid POP molecules in order to perform a comparison with the images of half size and double height presented in this work. The goal is to see if it we were dealing here with double-cuboid POPs broken into single-cuboid POP molecules and in addition to determine the adsorption geometry (e.g. up-right, flat, broken).
6. In order to perform the project shown in Figure 1.1 we suggest depositing POPs onto Cu(100) covered with 1 or 2 layers of $\text{Cu}(\text{NO}_3)_2$ to study POP adsorption on insulating rather than conductive substrates. The objective is to build substrates with gate electrodes.
7. POPs could be attached to single molecule magnet SMM via chemical bonds and then reduced to metallic Pd clusters. The next step will be the possibility of growing larger Pd or FePd nano-particles around the small Pd clusters.

Table 5.1 Summary of following tests and measurements as a follow-up to our work.

	Test or Technique	Objective
1	LEED	Characterize molecule arrays
2	Study of molecular arrays using STS	Look for internal structure of molecules and study electronic structure, e.g. HOMO-LUMO gap
3	POPs on Au (111) substrate	Check low concentrations and compare with HOPG
4	Different POP concentrations on HOPG using (STM, AES, XPS)	Observe transition from isolated molecules to islands and closed layers
5	Single-cuboid POPs	Address the adsorption geometry (up-right, broken, or flat).
6	POPs on Cu(100) covered with 1 or 2 layers of Cu(NO ₃) ₂ [Courtesy of Prof. Paul Kögerler, RWTH Aachen and FZJ]	POPs on insulating rather than metallic substrate. Towards substrates with gate electrode
7	POP attached to SMMs via chemical bonds then reduced to Pd clusters	If successful larger Pd or FePd nano-particles could be grown around the small Pd _x O species.

Bibliography

Chapter 1 Introduction

- [1][Whitesides and Love, 2001] G.M. Whitesides, J.C. Love, Nanotech, special issue of Sci. Am. 285 (2001).
- [2][Balzani et al. 2000] V. Balzani, A. Credi, F. M. Raymo, and J. F. Stoddart, Angew. Artificial molecular machines Chem. Int. Ed. 39, 3349 (2000).
- [3][Moore, 1965] G. E. Moore, 'Cramming more components onto integrated circuits', Electronics 38, 114 (1965).
- [4][ITRS, 2001] The semiconductor industries association, the international technology roadmap for semiconductors (<http://public.itrs.net>, 2001).
- [5][Special issue, 2000] the future of microelectronics, special issue in Nature 406, 1021 (2000).
- [6][Bogani and Wernsdorfer, 2008] Bogani, L. and Wernsdorfer, W. 'Molecular spintronics using single molecule magnets', Nat. Mat. 7(3), 179–186(2008)
- [7][Cleuziou et al. 2006] Cleuziou, J.-P., Wernsdorfer, W., Bouchiat, V., Ondarcuhu, T., and Monthieux, M. 'Carbon nano-tube superconducting quantum interference device', Nature Nanotech. 1, 53. (2006)
- [8][Roch et al. 2008] Roch, N., Florens, S., Bouchiat, V., Wernsdorfer, W., and Balestro, F. (2008) 'Quantum phase transition in a single-molecule quantum dot', Nature 453, 633 (2008).
- [9][Wolf et al. 2001] Wolf, S. A., Awschalom, D. D., Buhrman, R. A., Daughton, J. M., von Molnr, S., Roukes, M. L., Chtchelkanova, A. Y., and Treger, D. M. 'Spintronics: a spin-based electronics vision for the future', Science 294, 449 (2001).
- [10][Awschalom and FLatt, 2007] Awschalom, D. D. and Flatt, M. M. 'Challenges for semiconductor spintronics', Nature Phys. 3, 153–159. (2007)
- [11][Bogani and Wernsdorfer, 2008] L. Bogani and W. Wernsdorfer. 'Molecular Spintronics using Single-Molecule Magnets'. Nature Materials, 7:179–186, 2008.
- [12][Thomas et al. 2001] F. S. Thomas, N. S. Chen, L. P. Ford, and R. I. Masel, 'Vibrational/HREELS, UV/HREELS, and temperature-programmed desorption of benzene and hydrogen on (2×1) Pt (1 1 0)' Surf. Sci. vol. 486, page 1-8 (2001).
- [13][Chen et al. 2002] Q. Chen, D. J. Frankel, and N. V. Richardson, '[Chemisorption's induced chirality: glycine on Cu {1 1 0}](#)' Surf. Sci. vol.497, 37 (2002).
- [14] [Lukas et al. 2002] S. Lukas, G. Witte, and Ch. Wöll, 'Novel Mechanism for Molecular Self-Assembly on Metal Substrates: Unidirectional Rows of Pentacene on Cu (110) Produced by a Substrate-Mediated Repulsion' Phys. Rev. Lett. 88, 028301 (2002).

- [15][Meyer et al. 2001] F. J. Meyer zu Heringsdorf, M. C. Reuter, and R. M. Tromp, ‘Growth dynamics of pentacene thin films’ *Nature* 412, 517(2001).
- [16][Cui et al.2001] X. D. Cui, A. Primak, X. Zarate, J. Tomfohr, O. F. Sankey, A. L. Moore, T. A. Moore, D. Gust, G. Harris, and S. M. Lindsay, ‘Reproducible Measurement of Single-Molecule Conductivity’, *Science* 294, 571 (2001).
- [17][Nanoelectronics, 2005] ENIAC-Strategic Research Agenda, European Technology Platform Nanoelectronics, November, 2005, under <http://www.cordis.lu/ist/eniac>.
- [18][Ishikawa et al. 2004] N. Ishikawa, M. Sugita, T. Ishikawa, S. Koshihara, and Y. Kaizu. ‘Mononuclear Lanthanide Complexes with Magnetization Relaxation a Long Time at High Temperatures: A New Category of Magnets at the Single-Molecular Level’. *J. Phys. Chem. B*, 108:11265–11271, 2004.
- [19][Chiang et al .1994] H. J. Chiang, S in: Güntherodt and R. Wiesendanger. ‘Scanning Tunneling Microscopy’ I. Springer- Verlag, Berlin.
- [20][Jung et al. 1998] T. A. Jung, F. J. Himpsel, R. R. Schlittler, and J. K. in: R. Wiesendanger Gimzewski. ‘ Scanning Probe Microscopy’. Springer-Verlag, Berlin.(1998).
- [21][Fisher and Blochl, 1993] A. J. Fisher and P. E. Blochl. ‘Adsorption and scanning-tunneling-microscope imaging of benzene on graphite and MoS₂’, *Phys. Rev. Lett.*, 70:3263, 1993.
- [22][Song et al. 2002] I. K. Song, R. B. Shnitser, J. J. Cowan, C. L. Hill, and M. A. Barteau. ‘Nanoscale Characterization of Redox and Acid Properties of Keggin-Type Heteropoly-acids by Scanning Tunneling Microscopy and Tunneling Spectroscopy: Effect of Heteroatom Substitution’ *Inorg. Chem.*, 41:1292, 2002.
- [23][Song and Barteau, 2002] I. K. Song and M. A. Barteau. ‘Scanning Tunneling Microscopy (STM) and Tunneling Spectroscopy (TS) of Hetero-polyacid (HPA) Self-Assembled Mono-layers (SAMS): Connecting Nano Properties to Bulk Properties’, *Korean J. Chem. Eng.*, 19:567, 2002.
- [24][Song et al.2003] I. K. Song, J. E. Lyons, and M. A. Barteau. ‘Correlation of Alkane Oxidation Performance with STM and Tunneling Spectroscopy Measurements of Heteropolyacid Catalysts’ *Catalysis Today*, 81:137, 2003.
- [25][Kaba et al. 1998] M. S. Kaba, I. K. Song, D. C. Duncan, C. L. Hill, and M. A. Barteau. ‘[Molecular Shapes, Orientation, and Packing of Polyoxometalate Arrays Imaged by Scanning Tunneling Microscopy](#)’ *Inorg. Chem.*, 37,398-406, 1998.
- [26] [Song et al. 2002] I. K. Song, M. S. Kaba, and M. A. Barteau. ‘Nanoscale Investigation of Mixed Arrays of Keggin-Type and Wells-Dawson-Type Heteropolyacids (HPAs) by Scanning Tunneling Microscopy (STM)’ *Langmuir*, 18:2358, (2002)
- [27][Kaba et al. 2002] M. S. Kaba, I. K. Song, and M. A. Barteau. ‘Scanning tunneling microscopy (STM) and tunneling spectroscopy 106 *J. Phys. C (ST)* of heteropolyacid (HPA) self-assembled mono-layers (SAMS): connecting nano properties to bulk properties’ *J. Phys. Chem. B*, 2337, 2002.

- [28][Errington et al. 2005] R. J. Errington, S. S. Petkar, B. R. Horrocks, A. Houlton, L. H. Lie, and S. N. Patole. ‘Covalent Immobilization of a TiW₅ Polyoxometalate on Derivatized Silicon Surfaces’ *Angew. Chem. Int. Ed.*, 117:1280, 2005.
- [29][Feyter and Schryver, 2005] S. D. Feyter and F. C. D. Schryver. ‘Self-assembly at the liquid/solid interface: STM reveals’, *J. Phys. Chem. B*, 109:4290, 2005.
- [30][Hembacher et al. 2005] S. Hembacher, F. J. Giessibl, and J. Mannhart. ‘Local Spectroscopy and Atomic Imaging of Tunneling Current, Forces, and Dissipation on Graphite’ *Phys. Rev. Lett.*, 94:056101, 2005.
- [31][Barsukova-Stuckart et al. 2012] Barsukova-Stuckart, M.; Izarova, N. V.; Barret, R. A.; Wang, Z.; Van Tol, J.; Kroto, H. W.; Dalal, N. S.; Jiménez-Lozano, P.; Carbó, J. J.; Poblet, J. M.; von Gernler, M. S.; Drewello, T.; de Oliveira, P.; Keita, B.; Kortz, U. ‘Polyoxopalladates Encapsulating 8-Coordinated Metal Ions, [MO₈PdII₁₂L₈]_n (M = ScIII, MnII, FeIII, CoII, NiII, CuII, ZnII, LuIII; L = PhAsO₃₂-, PhPO₃₂-, SeO₃₂-)’, *Inorg. Chem.* 2012, 51, 13214-13228.
- [32][Nano-molecular science] <http://www.jacobs-university.de/ses/ukortz/research>
- [33] [Courtesy of Prof. Paul Kögerler, RWTH Aachen and FZJ] ERC project of Prof. Kögerler.

Chapter 2 Experimental Techniques

- [34][Binning and Rohrer, 2000] G. Binning and H. Rohrer, ‘scanning tunneling microscopy’, *IBM J. Res. Develop.* 44, (2000) 279-293.
- [35][Binning and Rohrer, 1986] G. Binning and H. Rohrer, ‘Scanning Tunneling Microscopy – From Birth to Adolescence’, *Nobel lectures* 1986.
- [36][IAP, 2012] http://www.iap.tuwien.ac.at/www/surface/stm_gallery/stm_schematic. February 2012
- [37][Bonnell, 2001] D. A. Bonnell, ‘Scanning Tunneling Microscopy and Spectroscopy – Theory, Techniques and Applications’, Wiley-VCH, New York 2001.
- [38][Besenbacher, 1986] F. Besenbacher, *Rep. Prog. Phys.* 59, (1996) 1737-1802.
- [39][Attocube] <http://www.attocube.com/nanoSCOPY/fundamentalsSTM.html>
- [40][Diehl et al. 2003] R D Diehl, J Ledieu, N Ferralis, A W Szmobdis and R McGrath, ‘Low-energy electron diffraction from quasicrystal surface’, *J. phys.: condens. Matter* 15 (2003) R63-R81.
- [41][Seah and Dench, 1979] M. P. Seah and W. A. Dench. ‘Quantitative electron spectroscopy of surfaces: A standard data base for electron inelastic mean free paths in solids’. *Surf. Interface Anal.*, 1, 1979.
- [42][Oura, 2003] K. Oura. ‘Surface Science’. Springer Verlag, 2003.

- [43][**Yan Bai, 2010**] Yan Bai, 'photoelectron spectroscopic investigation of porphyrins and phthalocyanines on Ag (111) and Au (111): Adsorption and Reactivity'. Nurnberg, Germany, 2010 (PhD)
- [44][**Omicron LEED**] <http://www.omicron.de/en/products/leed>
- [45][**Ertl and Koppers, 1974**] G. Ertl and J. Koppers, 'Low Energy Electrons and Surface Chemistry', (Verlag Chemie, Weinheim, 1974).
- [50][**Chang, 1971**] C. C. Chang, 'Auger electron spectroscopy', Surface Science 25, 53 (1971).
- [46][**Nesbitt and Pratt, 1995**] H. W. Nesbitt and A. R. Pratt, 'applications of Auger-Electron spectroscopy to geochemistry', The Canadian Mineralogist, Vol. 33, pp. 243-259(1995).
- [47][**Davis, 1976**] L. Davis "Handbook of Auger Electron Spectroscopy" (Physical Electronics, Eden Prairie, MN, 1976).
- [48][**Zangwill, 1988**] A. Zangwill, Physics at surfaces (Cambridge University Press, ADDRESS, 1988).

Chapter 3 Experimental Procedure

- [49][**Barsukova-Stuckart et al, 2011**] Barsukova-Stuckart, M.; Izarova, N. V.; Jameson, G. B.; Ramachandran, V.; Wang, Z.; van Tol, J.; Dalal, N. S.; Ngo Biboum, R.; Keita, B.; Nadjo, L.; Kortz, U. Angew. 'Synthesis and Characterization of the Dicopper (II)-Containing- 22-palladate (II) [Cu₂PdII₂₂P₁₂O₆₀ (OH) ₈]-20' Chem. 2011, 123, 2688-2692; Angew. Chem. Int. Ed. Engl. 2011, 50, 2639-2642.
- [50][**Chubarova et al. 2008**] E. V. Chubarova, M. H. Dickman, B. Keita, L. Nadjo, F. Miserque, M. Mifsud, I. W. C. E. Arends, U. Kortz, Angew. 'Self Assembly of a Heteropolyoxopalladate Nanocube, [PdII₁₃AsV₈O₃₄ (OH) ₆]-8-' Chem. Int. Ed. 2008, 47, 9542 – 9546.
- [51][**Izaroya et al. 2009**] N. V. Izarova, M. H. Dickman, R. Ngo Biboum, B. Keita, L. Nadjo, V. Ramachandran, N. S. Dalal, U. Kortz, 'Heteropoly-13-Palladates(II) [PdII₁₃(AsVPh)₈O₃₂]₆- and [PdII₁₃SeIV₈O₃₂]₆-' Inorg. Chem. 2009, 48, 7504 – 7506.
- [52][**N. V. Izarova et al. 2009**] N. V. Izarova, R. Ngo Biboum, B. Keita, M. Mifsud, I.W. C. E. Arends, G. B. Jameson, U. Kortz, Dalton Trans. 'Self-assembly of star-shaped heteropoly-15-palladate(II)' , 2009, 9385 – 9387;
- [53][**Barsukova-stuchart et al. 2010**] M. Barsukova, N. V. Izarova, R. Ngo Biboum, B. Keita, L. Nadjo, V. Ramachandran, N. S. Dalal, N. S. Antonova, J. J. Carb_, J. M. Poblet, U. Kortz, 'Polyoxopalladates Encapsulating Yttrium and Lanthanide Ions, [XIIIPdII₁₂(AsPh)₈O₃₂]₅- (X = Y, Pr, Nd, Sm, Eu, Gd, Tb, Dy, Ho, Er, Tm, Yb, Lu)', Chem. Eur. J. 2010, 16, 9076 – 9085.
- [54][**Kittel, 2005**] A. Kittel, Introduction to solid state physics, Jon Wiley & Sons, Danvers 2005.

- [55][Haiss et al. 1991] W. Haiss, D. Lackley, J. K. Sass, and K. H. Besocke. ‘Atomic resolution scanning tunneling microscopy images of Au (111) surfaces in air and polar organic solvents’. *Journal of Chemical Physics*, 95(3):2193–2196, 1991.
- [56] [Unertl, 1993] W. Unertl. *The Surface Structure of Crystalline Solids*, chapter 5, pages 107–154. In Bonnell [65], 1993.
- [57][Barth, 1990] V. Barth, H. Brune, G. Ertl, and R. J. Ben, ‘scanning tunneling microscopy observations on the reconstruction Au (111) surface: Atomic structure, long-range superstructure, rotational domains, and surface defects’, *Phys. Rev. B* 42, 9307-9318. (1990)
- [58][Woll et al. 1989] Ch. Woll, S. Chiang, R. J. Wilson, and P. H. Lippel. ‘Determination of atom positions at stacking-fault dislocations on Au (111) by scanning tunneling microscopy’. *Physical Review B*, 39:7988–7991, 1989.
- [59][Sandy et al. 1991] A. R. Sandy, S. G. J. Mochrie, D. M. Zehner, K. G. Huang and D. Gibbs, ‘Structure and phases of the Au(111) surface: X-ray-scattering measurements’ *Phys. Rev. B*, 43, 4667 (1991).
- [60][Min et al. 2005] B. K. Min, A. R. Alemozafar, M. M. Biener, J. Biener, and C. M. Friend, ‘Reaction of Au (111) with Sulfur and Oxygen: Scanning Tunneling Microscopic Study’ *Top. Catal.* 36, (2005) 77-90.
- [61][McNaught and Willinson, 1997] A.D. McNaught and A. Willinson, *IUPAC Compendium of Chemical Terminology 2nd Edition* (1997).
- [62][Shriver et al. 1994] D. F. Shriver, P. W. Atkins, C. H. Langford, *Inorganic Chemistry – 2nd edition*, Oxford University Press, Oxford New York 1994.
- [63][Batra, 1987] P. Batra, N. Garcia, H. Rohrer, H. Salemink, E. Stoll, and S. Ciraci, ‘[A study of graphite surface with STM and electronic structure calculations](#)’ *Surf. Sci.* vol.181, 126-138. (1987)
- [64][Ferralis et al. 2004] N. Ferralis, K. Pussi, S. E. Finberg, J. Smerdon, M. Lindroos, R. McGrath, and R. D. Diehl, ‘Low-energy electron diffraction study of potassium adsorbed on single-crystal graphite and highly oriented pyrolytic graphite’, *physical review B*, 70, 245407 (2004)

Chapter 4 Results

- [65][Matsui et al. 2005] Matsui, T.; Kambara, H.; Niimi, Y.; Tagami, K.; Tsukada, M.; Fukuyama, H. ‘STS Observations of Landau Levels at Graphite Surfaces’ *phys. Rev. Lett.* 2005, 94, 226403.

Polyoxopalladates on Au (111) and HOPG substrates

دراسة سلوك جزيئات بولي اوكسو بالاداتس ثنائية التكعيب على سطوح الذهب والجرافيت

إعداد: محمود الزير

إشراف

د. سلمان محمد سلمان دائرة الفيزياء جامعة القدس فلسطين

و د. دانييل بوغلر معهد غرانبيرغ بمركز يوليش بألمانيا

ملخص

تم دراسة إمكانية التصاق جزيئات بولي اوكسو بالاداتس ثنائية التكعيب على أسطح موصلات الذهب (111) و الجرافيت (اتش أو بي جي) لإمكانية تطبيقها كسلانف في الاليكترونيات المغناطيسية والتحقق منها .

وقد تم إيداع الجزيئات على السطوح من خلال التنقيط بقطرات من محلول الجزيئات على السطح وتركت لتبخّر المحلول مدة 1 ساعة في ظل الظروف المعيارية. وتم تشخيص السطوح بعد عملية الإيداع باستخدام كل من تقنيات (الأوجير) والمجهر النفقي. وأثبتت القياسات بواسطة الأوجير امكانية امتصاص السطوح المختارة للجزيء بطرق متفاوتة.

وتم تصوير الجزيئات بنجاح باستخدام المجهر النفقي حيث تم قياس بعض توزيعات الجزيئات بأبعاد أكبر كثيرا مقارنة مع حجم الجزيئات الفعلي على سطح الذهب (111) عند إيداع تركيز قليل. تجميع الجزيئات بهذا الشكل يجب أن يعتمد على التفاعل الذاتي ما بين الجزيئات وما بين الجزيئات والسطح.

إيداعات الجزيئات على سطح (اتش أو بي جي) كانت أكثر نجاحا. حيث تم التصوير بدقة عالية لجزيئات سليمة باتجاهات مختلفة وترتيبات متعددة في مصفوفات وسلاسل منظمة في بعض الحالات. واتبعت المصفوفات بنية السطح بينما وقعت السلاسل على طول حواف المصفوفات

هناك حاجة إلى مزيد من البحث للحصول على فهم أكثر تحديدا لمختلف التكوينات والتوزيع وتفسير الحالات الشاذة من خلال تصوير المجهر النفقي بتركيزات أقل ودراسات بالتفصيل للإيداع باستخدام (الأوجير) إضافة إلى توصيات بقياسات من أجل دراسة الجوانب الأخرى للتطبيقات الممكنة.